



Cite this: *Sens. Diagn.*, 2023, 2, 361

Recent advances in MoS₂-based nanomaterial sensors for room-temperature gas detection: a review

Xu Tian,^a Shanli Wang,^a Haoyu Li,^a Mengyao Li,^a Ting Chen,^{*b}
 Xuechun Xiao^{*a} and Yude Wang ^{*c}

The two-dimensional (2D) material, MoS₂, has attracted great attention in the development of room-temperature gas sensors in recent years due to its large specific surface area, ultra-high carrier mobility, strong surface activity, and high adsorption coefficient. However, pristine MoS₂ gas sensors still exhibit some drawbacks such as low sensing response, sluggish recovery process, and incomplete recovery, which are unfavorable for the application of gas sensors. Therefore, significant efforts have been devoted to the design of specific MoS₂-based gas sensors with enhanced sensing properties. In this review, we aim to discuss the recent advances in MoS₂-based nanomaterial sensors for room-temperature gas detection. Firstly, some strategies to improve the gas sensing performance of MoS₂-based gas sensors are introduced, including designing morphologies, creating sulfur vacancies, decorating noble metals, doping elements, introducing light, and constructing composites. Secondly, the types of gases that can be detected by MoS₂-based gas sensors are proposed and summarized, and their sensing mechanisms are also analyzed. Finally, an outlook is presented and the future research directions and challenges are discussed.

Received 17th November 2022,
 Accepted 22nd December 2022

DOI: 10.1039/d2sd00208f

rsc.li/sensors

1. Introduction

The detection of toxic and harmful gases is important to ensure the safety of life and protect the environment. In the past few decades, semiconductor metal oxide (SMO) gas sensors have been the dominant tools for the detection of toxic gases such as volatile organic compounds (xylene, toluene, formaldehyde (HCHO), ammonia (NH₃), acetone, ethanol, methanol, and isopropanol), flammable and explosive gases (methane (CH₄), hydrogen (H₂), propane (C₃H₈), carbon monoxide (CO), hydrogen sulfide (H₂S)), nitrogen oxides (nitrogen monoxide (NO), nitrogen dioxide (NO₂)), sulfur oxides (sulfur dioxide (SO₂)), and carbon oxides (carbon dioxide (CO₂)). To date, SMO gas sensors still occupy the central position in the field of gas detection due to their high sensing response, fast response/recovery time and excellent reproducibility. However, some deficiencies

presented by SMO gas sensors include their poor selectivity and high operating temperature, which have not been addressed to date. In particular, their high operating temperature will be detrimental to energy saving and limit their application in some special fields. Therefore, it is necessary to develop low-power, high-sensing performance gas sensors.

Recently, several reports have revealed that the emerging two-dimensional (2D) materials exhibit a sensing response to toxic gases at low/room temperature, which not only solves the problem of high power consumption of traditional gas sensors to a certain extent but also enable them to be applied in flexible wearable electronic devices to provide great convenience and achieve intelligent life. The 2D materials include reduced graphene oxide (rGO),¹ transition metal dichalcogenides (TMDs),² black phosphorus (BP),³ hexagonal boron nitride (h-BN),⁴ and transition metal carbides, nitrides and/or carbonitrides (MXenes),⁵ which can be considered as promising gas sensing materials owing to their unique single-atom layer structure. Specifically, they exhibit high specific surface area close to the theoretical extreme, excellent semiconductor performance, unique surface configurations with dangling bonds on their edge sites, and flexible basal planes.^{6–10} Among them, the layered TMDs with the composition of MX₂ (M = Ti, Zr, Hf, V, Nb, Ta, Mo, W, Tc, Re, Pd, and Pt and X = S, Se, and Te)¹¹ have gained intensive attention as gas sensing materials because of their strong

^a National Center for International Research on Photoelectric and Energy Materials, School of Materials and Energy, Yunnan University, 650091 Kunming, People's Republic of China. E-mail: xchxiao@ynu.edu.cn; Fax: +86 871 65153832; Tel: +86 871 65035570

^b Institute of Materials Science & Devices, School of Materials Science and Engineering, Suzhou University of Science and Technology, Suzhou, 215009, People's Republic of China. E-mail: chenting@mail.usts.edu.cn

^c Key Lab of Quantum Information of Yunnan Province, Yunnan University, 650091 Kunming, People's Republic of China. E-mail: ydwang@ynu.edu.cn



spin-orbit coupling interaction, tunable electronic properties, and high interaction ability for the adsorption of gas molecules.^{12,13} Among the TMDs, the semiconductor MoS₂ and WS₂ with atomically thin-layered structures, lower bandgap, abundant edge active sites, and excellent electrical and/or chemical properties exhibit good gas sensing abilities at room temperature (RT).^{14–16} In particular, MoS₂ has become the most ideal gas sensing material^{17,18} owing to its ultra-high carrier mobility, high adsorption coefficient, tunable bandgap (1.2–1.9 eV), and excellent field-effect transistor behavior.^{19–22} These parameters have a positive impact on the sensitivity and stability of gas sensors and the designability of novel sensing materials based on MoS₂. MoS₂ presents four crystal structures including 1H, 1T, 2H, and 3R, which are defined by the coordination relationship between the Mo and S atoms and the stacking order between their layers, as shown in Fig. 1. The numbers 1, 2, and 3 represent the number of S–Mo–S layers in each unit cell, while the letters T, H, and R represent triangle, hexagonal, and rhombohedral, respectively. The 1T-MoS₂ phase shows metallic nature, whereas the 2H-MoS₂ phase exhibits semiconductor characteristic (n-type). In terms of thermodynamics, besides the 2H phase, three other crystal phases of MoS₂ possess a metastable structure, which can also be transformed under certain conditions.²³ Therefore, the thermodynamically stable 2H-MoS₂ structure dominates current applications.²⁴

Recently, several review papers highlighted 2D layered material-based resistive sensors.^{8,25,26} These works emphatically discussed the synthesis methods, gas sensing application of TMDs, and the sensing mechanisms of TMDs van der Waals nanocomposite junctions. Considering the advantages of MoS₂ and its potential application in developing room-temperature gas sensors, herein, we mainly review the recent advances of MoS₂ nanomaterial-based gas

sensors for room temperature detection. Based on the existing review papers, we further present the development of MoS₂ gas sensors and discuss them in detail. Initially, we discuss some strategies for improving the gas sensing properties of MoS₂. Subsequently, we summarize the types of toxic gases that MoS₂ can sense at RT. Moreover, the sensing mechanisms of MoS₂-based gas sensors towards different gases are also discussed. Furthermore, we conclude this review with some perspectives and outlooks on this new trend in the field of gas sensing.

2. Strategies to improve the gas sensing performance of MoS₂

Although MoS₂ has shown great advantages in the development of room temperature gas sensors, it still faces some challenges, for instance, due to the stacking of the S–Mo–S layers, bulk MoS₂ does not have sufficient contact with gas molecules and forms poor conductive network signals, which lead to a low response value and slow response recovery rate. Especially, the incomplete recovery at RT is a severe challenge for MoS₂-based gas sensors. In this regard, more efforts have been devoted to designing specific MoS₂-based RT gas sensors with enhanced sensing properties. The improvement strategies include designing morphologies, creating sulfur vacancies, decorating noble metals, doping elements, introducing light, and constructing composites. In this part, we summarize the above-mentioned strategies for improving the gas sensing performance of MoS₂ materials.

2.1 Morphology design

For sensing applications, the morphology of MoS₂ plays a crucial role in enhancing the sensing performance by providing more reactive sites. A change in the morphology of

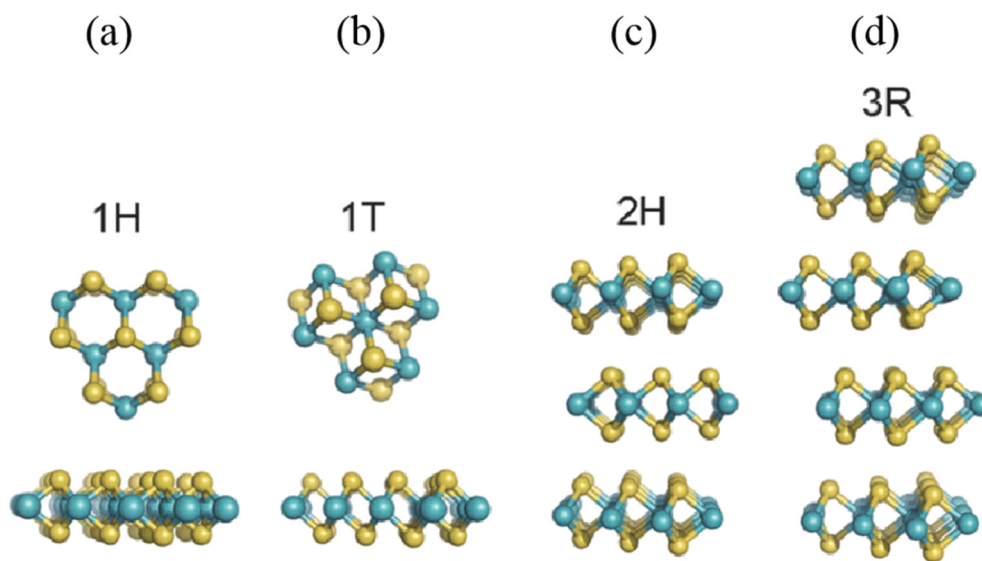


Fig. 1 Different polymorphs or phases of MoS₂: (a) 1H phase, (b) 1T phase, (c) 2H phase, and (d) 3R phase. Reprinted with permission from ref. 24. Copyright 2015, The Royal Society of Chemistry.



MoS₂ refers to its dimensions, which can be varied from zero, one, and two to three-dimensional nanostructures. MoS₂ with different dimensions exhibit unique physical and optoelectronic properties, defects, exposed facets, porosity, atomic configuration,²⁷ and thus its gas sensing properties will also be different. When MoS₂ is compressed to zero-dimensional, completely special electronic and photophysical properties are generated due to the quantum confinement and edge effects,²⁸ such as a higher direct bandgap of 3.96 eV,²⁵ larger edge-to-volume ratio, and higher in-plane

electron transport rate. Niu *et al.*²⁹ synthesized MoS₂ quantum dots (MQDs) *via* the combined high speed shear, sonication and solvothermal treatment of bulk MoS₂ in *N,N*-dimethylformamide. Fig. 2a shows the HRTEM image of MQDs with an average size of 7.8 nm. NH₃ and NO₂ gases were recognized by the MQD sensor at RT. The dynamic sensing response of the MQD sensor towards various concentrations of NO₂ (Fig. 2b) and NH₃ (Fig. 2c) revealed that it had almost the same response value for both gases. However, the recovery was not complete due

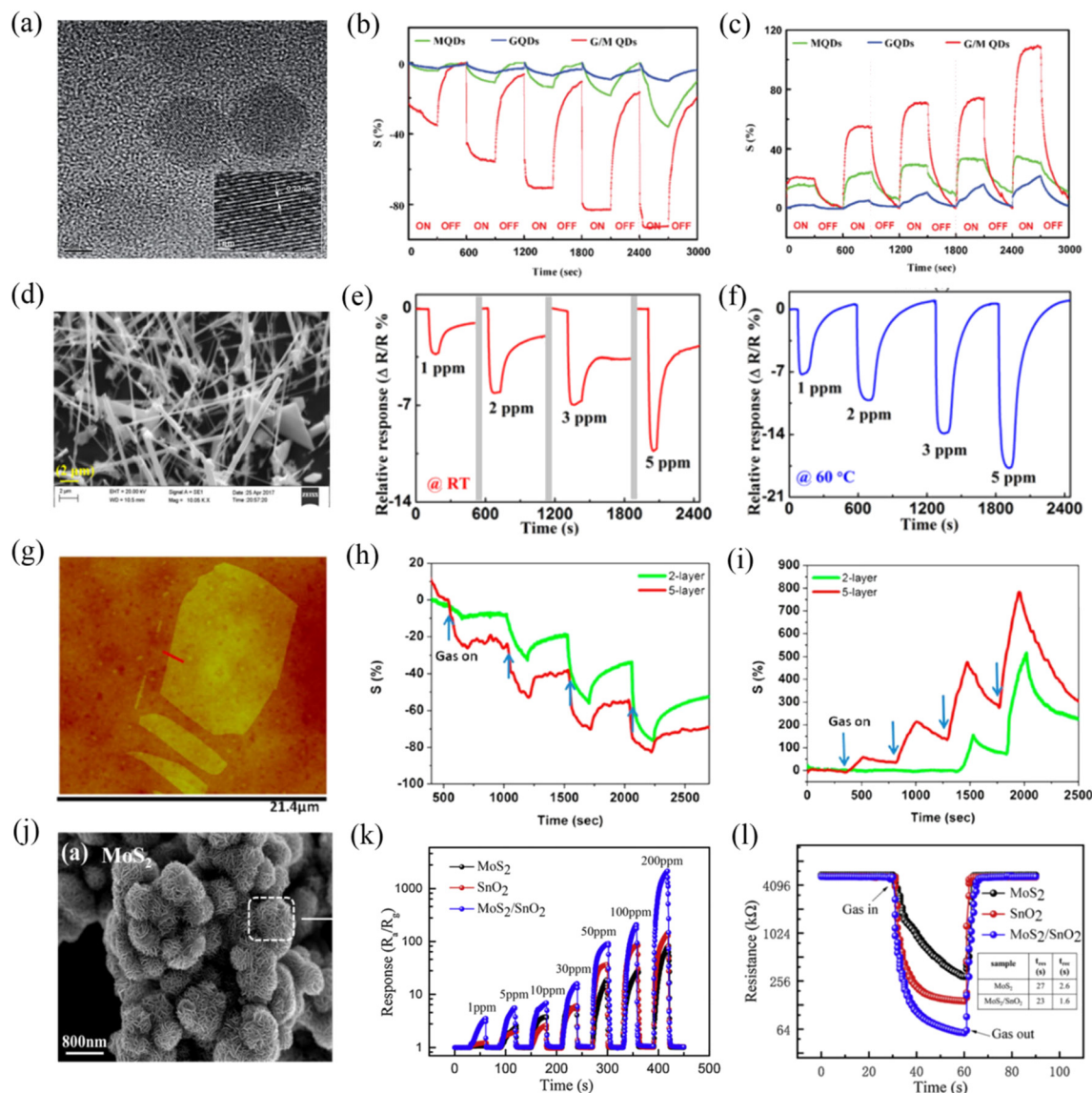


Fig. 2 (a) HRTEM of MQDs. Dynamic response of the MQDs (green) upon exposure to increasing (b) NO₂ and (c) NH₃ concentrations. Reprinted with permission from ref. 29. Copyright 2016, The Royal Society of Chemistry. (d) SEM image of MoS₂ nanowires. Transient response of the MoS₂ nanowire sensor at (e) room temperature (RT) and (f) 60 °C. Reprinted with permission from ref. 30. Copyright 2018, AIP Publishing. (g) AFM image of single-layer MoS₂ sheet. Comparative two- and five-layer MoS₂ cyclic sensing performances with (h) NH₃ and (i) NO₂ (for 100, 200, 500, and 1000 ppm). Reprinted with permission from ref. 31. Copyright 2013, the American Chemical Society. (j) SEM images of MoS₂ nanoflowers. (k) Responses curves of MoS₂, SnO₂, and SnO₂/MoS₂ sensors to various concentrations (1–200 ppm) of NH₃. (l) Resistance curves of MoS₂, SnO₂, and SnO₂/MoS₂ to 50 ppm of NH₃ at room temperature (the insert table indicates the response and recovery times). Reprinted with permission from ref. 33. Copyright 2020, Elsevier B.V.

to the high-energy binding sites of the MQDs. This research team is working on how to balance the relationship between the selectivity and fast desorption in their further study.

One-dimensional MoS₂ nanostructures include nanowires and nanotubes. Their electronic properties also vary with a change in their diameter and chirality, for example, MoS₂ nanotubes exhibit a larger bond length and smaller semiconducting bandgap than that of the bulk MoS₂ nanosheets.²⁵ Kumar *et al.*³⁰ reported the fabrication of an NO₂ sensor based on one-dimensional MoS₂ nanowires (Fig. 2d), which were synthesized using chemical transport reaction through controlled turbulent vapor flow. The results showed that the MoS₂ nanowire sensor displayed a high sensing response to NO₂ gas; however, it still faced the problem of incomplete recovery at RT due to the strong binding between NO₂ and the reactive sites of MoS₂, as shown in Fig. 2e. Thus, to address its difficult recovery and low response at RT, this team investigated its sensing behavior at a high operating temperature (60 °C) (Fig. 2f). They proposed that the relatively quick adsorption and desorption of NO₂ gas molecules from MoS₂ at 60 °C were attributed to its high conductivity and the rapid interaction of gas molecules with the exposed edge sites of the nanowires. Also, they indicated that the oxygen and humidity occupy a large number of reactive sites in the MoS₂ nanowires at RT, and thus there were less NO₂ molecules to participate in the reaction, resulting in a weak response to NO₂ at RT.

MoS₂ with monolayer or few-layer two-dimensional nanostructures is currently the most studied in the field of gas sensing. Monolayer MoS₂ shows a direct bandgap of 1.8 eV, while bulk MoS₂ possesses an indirect bandgap of 1.2 eV. This transition endows monolayer MoS₂ with superior semiconductor properties. Meanwhile, monolayer or few-layer MoS₂ expose abundant edge sites and a high specific surface area, which may be beneficial for the absorption of gas molecules. In addition, it also exhibits high toughness and has potential to be applied on flexible substrates. Late *et al.*³¹ investigated whether the single-layer MoS₂ is an ideal structure for enhancing the gas sensing performances. The AFM image of single-layer MoS₂ is shown in Fig. 2g. They found that the single-layer MoS₂ device was not stable over time. For clarity and brevity, they examined the gas sensing responses of two-layer and five-layer MoS₂ to various concentrations of NH₃ (Fig. 2h) and NO₂ (Fig. 2i) gases at RT because they were the thinnest and the thickest, respectively. The results showed that five-layer MoS₂ had better sensitivity compared to that of the two-layer MoS₂, they agreed that this may be due to the different electronic structures with a variation in thickness (layering). However, this issue is complicated and needs further study. Li *et al.*³² prepared few-layer MoS₂ nanosheets *via* mechanical exfoliation for the RT detection of NO₂. This sensor achieved high responsivity and ultrafast recovery behavior to NO₂. They proposed that the high sensitivity was caused by the thin thickness of MoS₂,

while the fast recovery time was attributed to the weak van der Waals force between NO₂ and MoS₂.

Three-dimensional nanoflower-like MoS₂ (Fig. 2j) assembled by several nanosheets has also received great attention for gas sensing. MoS₂ nanoflower is mainly synthesized *via* a hydrothermal process. Wang *et al.*³³ prepared MoS₂ nanoflowers *via* a simple hydrothermal method at 200 °C for 22 h. Fig. 2k shows the dynamic sensing response curves of MoS₂, SnO₂, and SnO₂/MoS₂ sensors towards different concentrations of NH₃ at RT. It was observed that the nanoflower-structured MoS₂ and its nanocomposite-based gas sensors exhibited high sensing response values. The resistance curves (Fig. 2l) of the MoS₂, SnO₂, and SnO₂/MoS₂ sensors exposed to 50 ppm NH₃ revealed that they displayed a very fast response and recovery rate (27/2.6 s for MoS₂ sensor), which seems to be very interesting. Thang *et al.*³⁴ discussed the effect of the hydrothermal growth times of 24, 36, 48, and 60 h on the sensitivity of the obtained MoS₂ nanoflowers and concluded that 48 h was the best growth time. The 48 h-MoS₂ nanoflowers showed a high gas response of 67.4% and high selectivity to 10 ppm NO₂ at RT. The superior sensing performance of the 48 h-MoS₂ nanoflower was ascribed to its largest specific surface area, smallest crystallite size, and lowest activation energy among the prepared samples. The dynamic resistance characteristic revealed that the 48 h-MoS₂ sensor exhibited complete response and recovery to NO₂ gas at RT. The authors ascribed this result to the high specific surface area and defects of the 48 h-MoS₂. They proposed that several factors such as high specific surface area, defective/strained surface, and weak van der Waals binding between the target gas and the MoS₂ surface affected the gas adsorption and desorption behavior. However, the complete recovery mechanism of the MoS₂ sensor is a complex case, and there are some disputes due to the combined effects of physi- and chemi-sorption, role of defects sites and transduction mechanism.³⁵

2.2 Vacancy promotion

The lack of adsorption sites in MoS₂ has become the main bottleneck in realizing a high sensing performance at RT. It has been theoretically and experimentally proven that the vacancies in MoS₂ act as high-energy binding sites and play an important role in enhancement the gas sensing performance. The vacancies mainly refer to two types, *i.e.*, Mo vacancy and S vacancies. However, the lower binding energy of S vacancy (2.12 eV) compared to Mo vacancy (6.20 eV) makes its construction more desirable, wherein the S vacancy is defined as the absence of one or two sulfur atoms per MoS₂.^{36,37} The strategy of generating S vacancies in MoS₂ aims to reduce the Gibbs free energy of gas adsorption,³⁸ increase the amount of charge transfer,³⁹ facilitate molecular adsorption and chemical functionalization,⁴⁰ offer abundant active sites, and even cause the dissociation of gas molecules.⁴¹ At present, S vacancies can be achieved by



microwave-hydrothermal treatment, liquid-phase ultrasonic exfoliation, metal quantum dot loading,⁴² electron irradiation and thermal annealing.^{36,43,44}

Xia *et al.*⁴³ discussed the NO₂ gas sensing performance of conventional MoS₂ (C-MoS₂) and sulfur-vacancy-enriched MoS₂ (SV-MoS₂) under dark and near-infrared (NIR) light conditions at RT, respectively. The researchers employed X-ray diffraction (XRD), electron paramagnetic resonance (EPR), and X-ray photoelectron spectroscopy (XPS) characterization techniques to prove the presence of sulfur vacancies, enriched S vacancy defects, and defect-related surface species in the MoS₂ samples, as shown in Fig. 3a–c, respectively. The response in Fig. 3d reveals that the SV-MoS₂ sensor showed a better gas sensing performance to 200 ppm NO₂ than the C-MoS₂ sensor in both the dark and under NIR illumination, which can be ascribed to the presence of more active centers and increased electron transfer introduced by the S vacancies. Moreover, the response value of the SV-MoS₂ sensor under NIR light had a significant improvement compared to that in a dark environment, while a slight increase occurred in the C-MoS₂ sensor, demonstrating that the S vacancy-induced photocurrent could effectively detect NO₂ gas at RT.

Zhang *et al.*⁴⁵ introduced S vacancies in 2D-in-3D architecture MoS₂ by high temperature annealing in an argon atmosphere. They compared the sensing properties of different MoS₂ samples obtained at various annealing

temperatures of 0 °C, 550 °C, 700 °C, and 850 °C to NO₂ at RT. The results showed that the hierarchical MoS₂ annealed at 850 °C exhibited an extremely high gas sensing performance in terms of sensitivity (Fig. 3e), selectivity and stability. These excellent sensing properties can be attributed to the large number of S vacancies in MoS₂, which were generated upon high temperature annealing and led to the strong interlayer coupling and spin–orbit coupling effects. The generation of S vacancies was confirmed by the decrease in the S:Mo ratio (Fig. 3f) under high temperature annealing by XPS measurements. In this regard, S vacancies play an extremely important role in improving the gas sensing performance of MoS₂ materials.

In addition, density functional theory (DFT) calculations also revealed that MoS₂ rich in S vacancies possessed a higher sensing performance to gases. Li *et al.*⁴⁶ calculated the adsorption properties and charge transfer of NO molecules on monolayer MoS₂ (MoS₂-MLs), S vacancy-defective MoS₂-MLs (S-vacancy), and vacancy complex of Mo and its nearby three sulfur vacancies (MoS₃-vacancy) by density functional theory (DFT). The adsorption energy of an NO molecule on the most stable adsorption models of MoS₂-MLs, S-vacancy, and MoS₃-vacancy was 0.14 eV, 2.57 eV and 1.95 eV, respectively. The theoretical results demonstrated that the MoS₃-vacancy and S-vacancy-defective MoS₂-MLs showed stronger chemisorption and greater electron transfer effects than pure MoS₂-ML,

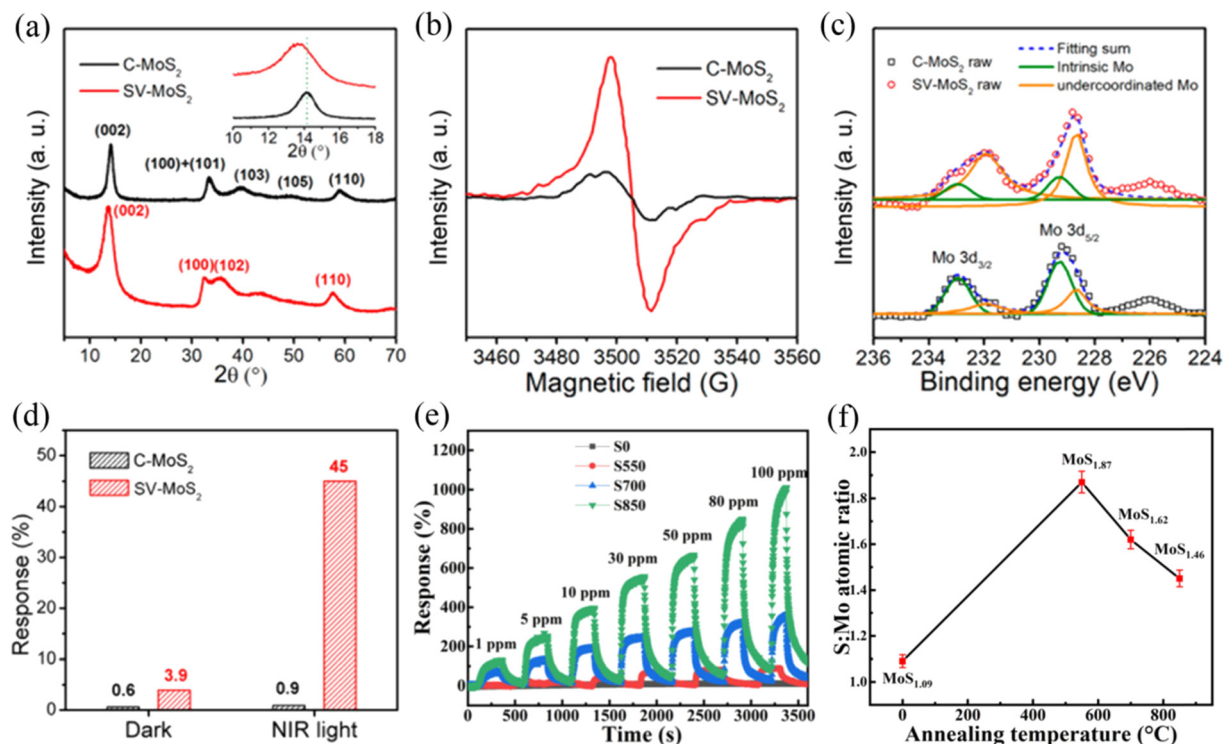


Fig. 3 (a) XRD, (b) EPR, (c) Mo 3d XPS spectra of C-MoS₂ and SV-MoS₂ samples. (d) Gas responses of C-MoS₂ and SV-MoS₂ sensors in the dark and under NIR illumination. Reprinted with permission from ref. 43. Copyright 2019, the American Chemical Society. (e) Dynamic response curves of the S0, S550, S700, and S850 sensors toward different concentrations of NO₂ at room temperature. (f) Corresponding S:Mo atomic ratio of S0, S550, S700, and S850. Reprinted with permission from ref. 45. Copyright 2022, Elsevier B.V.

implying that S-vacancy defects can effectively improve the NO sensing performance of MoS₂.

Although the vacancies on the surface of MoS₂ acts as active sites for the adsorption of gas molecules, their high adsorption energy will also result in a slow response and recovery rate.³⁵

2.3 Noble metal decoration

The decoration of noble metals (NMs) on MoS₂ has also been reported as another effective strategy to improve its gas sensing properties. NMs such as Au, Ag, Pt, Pd, Rh, and Ru are usually used as effective catalysts to enhance the surface reactivity of sensing materials and accelerate the reaction between the adsorbed oxygen species and the gas molecules.⁴⁷ Meanwhile, they can also change the electron accumulation and enhance the electron transfer due to the different work functions between the NMs and sensing materials. Moreover, NMs possess affinity for some specific gas molecules and assist in overcoming the problem of selectivity to a certain extent.⁴⁸

Jaiswal *et al.*⁴⁹ reported the preparation of a vertically aligned edge-oriented MoS₂ hybrid nanostructured thin film decorated with Pd nanoparticles (Pd/MoS₂) on quartz and Si substrates using the DC magnetron sputtering technique. The 2D and 3D AFM micrographs of the Pd-functionalized vertically aligned MoS₂ thin film are shown in Fig. 4a and b, respectively. The Pd/MoS₂ hybrid film sensor exhibited an enhanced response of 33.7% and fast response/recovery rate

(~16/38 s) compared to the pristine MoS₂ thin film sensor (1.2% response value and ~29/158 s response/recovery time) to 500 ppm H₂ gas at RT (Fig. 4c). The enhancement in the H₂ gas sensing performance of the Pd/MoS₂ hybrid film sensor can be attributed to three aspects. Firstly, the catalytic activity of the small Pd nanoparticles endowed the hydrogen molecules with efficient decomposition ability. Secondly, the unique porous nanostructure of the vertically aligned edge-enriched MoS₂ possessed a higher specific surface area. Finally, the Schottky barrier at the junction between Pd and MoS₂ increased the electrical resistance in air due to the barrier height, becoming more sensitive to a change in H₂ resistance.

Halvae *et al.*⁵⁰ synthesized Ag/MoS₂ nanorods *via* the hydrothermal method. This sensor displayed a selective sensing response for methanol vapor at RT. Firstly, the researchers discussed the effect of different amounts of Ag nanoparticles on the response of the sensor. They found that the mass ratio of 2 wt% Ag nanoparticles loaded on MoS₂ resulted in the best methanol sensing response. The improved gas sensing properties can be ascribed to the catalytic oxidation and chemical sensitization of Ag nanoparticles. Meanwhile, the selectivity of Ag/MoS₂ to methanol was much better than that of pure MoS₂. In addition to the small size of methanol, which could easily penetrate the layered MoS₂, Ag had a better decoration effect to improve the selectivity.

Park *et al.*⁵¹ prepared two-dimensional MoS₂ *via* a metal organic chemical vapour deposition (MOCVD) method, and

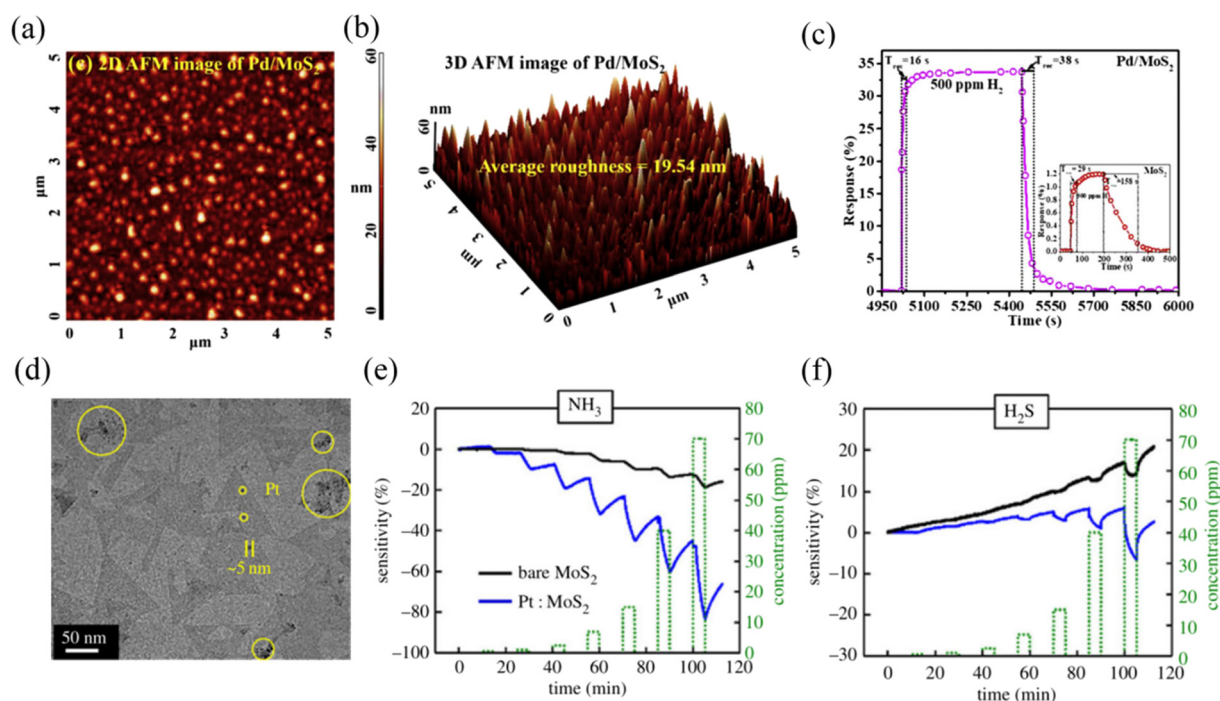


Fig. 4 (a) 2D and (b) 3D AFM micrographs of Pd-functionalized vertically aligned MoS₂ thin film. (c) Sensor response curve of the Pd/MoS₂ hybrid and pristine MoS₂. Reprinted with permission from ref. 49. Copyright 2020, Elsevier B.V. (d) TEM images of the Pt/MoS₂. Gas-sensing characteristics of the MoS₂ and Pt/MoS₂ gas sensors for (e) NH₃ and (f) H₂S. Reprinted with permission from ref. 51. Copyright 2020, IEEE Xplore.



subsequently modified its surface with Pt particles (Fig. 4d). Pt particles have a double p-type doping effect compared to Au particles and possess good corrosion and oxidation resistance. Accordingly, this sensor recognized both NH_3 and H_2S gases at RT; however, the response for H_2S was lower than that for NH_3 , as shown in Fig. 4e and f, respectively, confirming that there was less charge transfer between H_2S and Pt/ MoS_2 . Meanwhile, the response value of Pt/ MoS_2 for the target gases was higher than that of bare MoS_2 , demonstrating that the Pt particles made an excellent contribution to the improvement in gas sensing performance.

2.4 Element doping

Element doping refers to a change in lattice constant due to the incorporation of dopants in the lattice of MoS_2 or replacement of the Mo, S lattice sites. In this process, the binding energy will be greatly enhanced and defects will be formed to become new active sites, and the electrical properties will also be changed due to the decrease in the electron-hole recombination rate.⁵² The doped elements can be divided into metal and nonmetal, where the metal dopants include Zn, W, Nb, Fe, Co, Ni, Cu, Ti, V, Ta, Al, and Ga,^{45,53–58} and nonmetal dopants include N, Si, B, N, P, and

Cl.^{59–61} However, most doping strategies focus on theoretical calculations based on density functional theory (DFT),^{62–65} where theoretical results reveal that doped- MoS_2 sensors exhibit a higher adsorption energy, stronger noncovalent interaction, greater carrier transport number, and faster conductivity rate to target gases.^{60,62,63} Therefore, more efforts should be devoted to the experimental exploration of doping MoS_2 . At present, some experimental studies have been reported.

Wu *et al.*⁵⁹ designed an N element-doped MoS_2 gas sensor by controlling the solvothermal temperature to realize the conversion of MoS_2 from n-type to p-type. The researchers proposed that doping could also address the challenge of sluggish sensing of MoS_2 at RT owing to the adjustable active sites and electrical property. Fig. 5a displays the gas sensing response value of pristine MoS_2 and optimal N-doped MoS_2 ($\text{NMoS}_2\text{-2}$) sensors to various concentrations of NO_2 at RT. It was observed that the $\text{NMoS}_2\text{-2}$ sensor showed obvious p-type semiconductor feature because the N atoms have one less valance electron than the S atoms in the MoS_2 matrix. Meanwhile, the sensing response value of the $\text{NMoS}_2\text{-2}$ sensor was not obviously improved compared to that of the pristine MoS_2 . However, the fast response/recovery rate (Fig. 5b and c) of the $\text{NMoS}_2\text{-2}$ sensor revealed that there was a superior fast charge transfer character, as confirmed by the

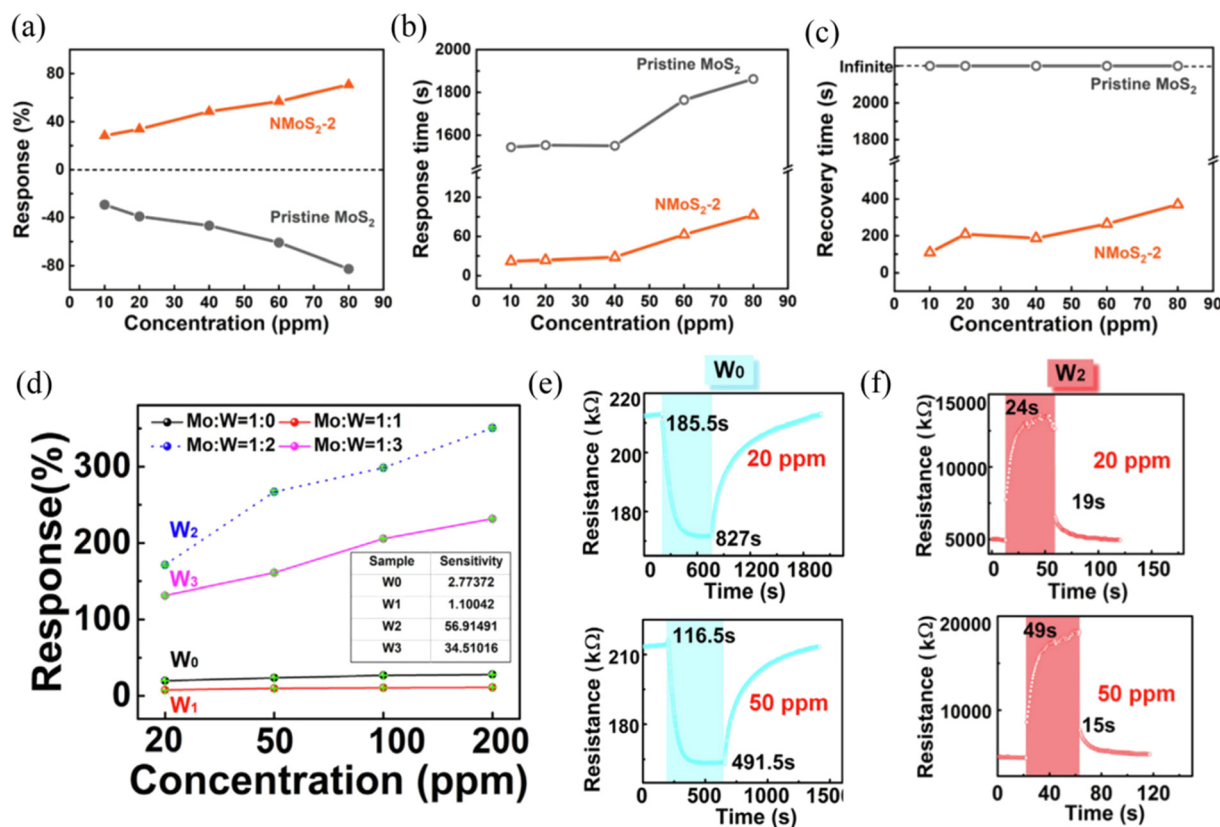


Fig. 5 (a) Response, (b) response time, and (c) recovery time of $\text{NMoS}_2\text{-2}$ and pristine MoS_2 upon exposure to 10, 20, 40, 60, and 80 ppm NO_2 . Reprinted with permission from ref. 59. Copyright 2021, Elsevier B.V. (d) Response value versus NO_2 concentration for W_0 – W_3 . (e) Transient response characteristic of (e) W_0 and (f) W_3 at 20 and 50 ppm NO_2 . Reprinted with permission from ref. 53. Copyright 2020, Elsevier B.V.

Hall effect. DFT calculations revealed that there was a favorable surface interaction between the N-doped MoS₂ and NO₂ molecules after N doping. Therefore, N-doping in MoS₂ resulted in a significant improvement in NO₂ sensing response/recovery ability.

Liu *et al.*⁵³ synthesized W-doped MoS₂ sensors with different W ratios *via* a hydrothermal method. The results showed that appropriate ratios between Mo and W were conducive to enhancing the NO₂ sensing properties at RT. As shown in Fig. 5d, when the Mo:W ratio was 1:2 (named W₂), the sensing response was observed to be the best for various concentrations of NO₂. Furthermore, the response/recovery times of the W-doped MoS₂ (W₂) sensor (Fig. 5f) was greatly improved compared to the undoped MoS₂ sensor (Fig. 5e), which was mainly attributed to the effective suppression of defects by W doping.

Briefly, according to the current research results, the doping method can be regarded as an effective method to solve the slow response/recovery ability of MoS₂.

2.5 Light assistance

Light assistance has shown promise for the activation of gas sensor materials. MoS₂ possesses a tunable band gap and excellent photoelectrical properties, and thus it is also an effective way to improve its gas sensing performance by light activation. Light activation mainly assists the recovery rate of

MoS₂ gas sensors,⁶⁶ and the photochemical reaction occurring between the light-generated electron/hole carriers in MoS₂ and adsorbed gas molecules promotes the desorption process.^{67,68} At present, two light activation gas sensing mechanisms have been proposed, *i.e.*, the “optoelectronic” and “photocatalytic” mechanisms. The optoelectronic mechanism refers to the generation of a photocurrent, which regulates the conductivity of the material and causes a large change in the resistance of the sensor upon gas exposure.^{15,69} The photocatalytic mechanism considers the process of photocatalytic oxidation of reducing gases into NO_x, CO₂ and H₂O,^{70,71} thus accelerating the chemisorption reaction between the sensing material and target gases.

Wang *et al.*⁷² proposed the visible-light photocatalytic enhancement gas sensing mechanism based on MoS₂/rGO hybrids for the detection of formaldehyde (HCHO) at RT. The comparison of response/recovery times of the MoS₂/rGO sensor to 10 ppm HCHO in the dark and under visible-light illumination, as shown in Fig. 6a, which revealed that the visible light accelerated the gas molecule adsorption/desorption process. In addition, the O₂-TPD spectra of MoS₂, as shown in Fig. 6b, demonstrated that visible light induced the adsorption of more oxygen species. Meanwhile, CO₂ peaks at 1358 and 1572 cm⁻¹ and broad H₂O peak at around 3420 cm⁻¹ were observed by *in situ* IR spectroscopy (Fig. 6c) when MoS₂ was exposed to HCHO and illuminated by visible

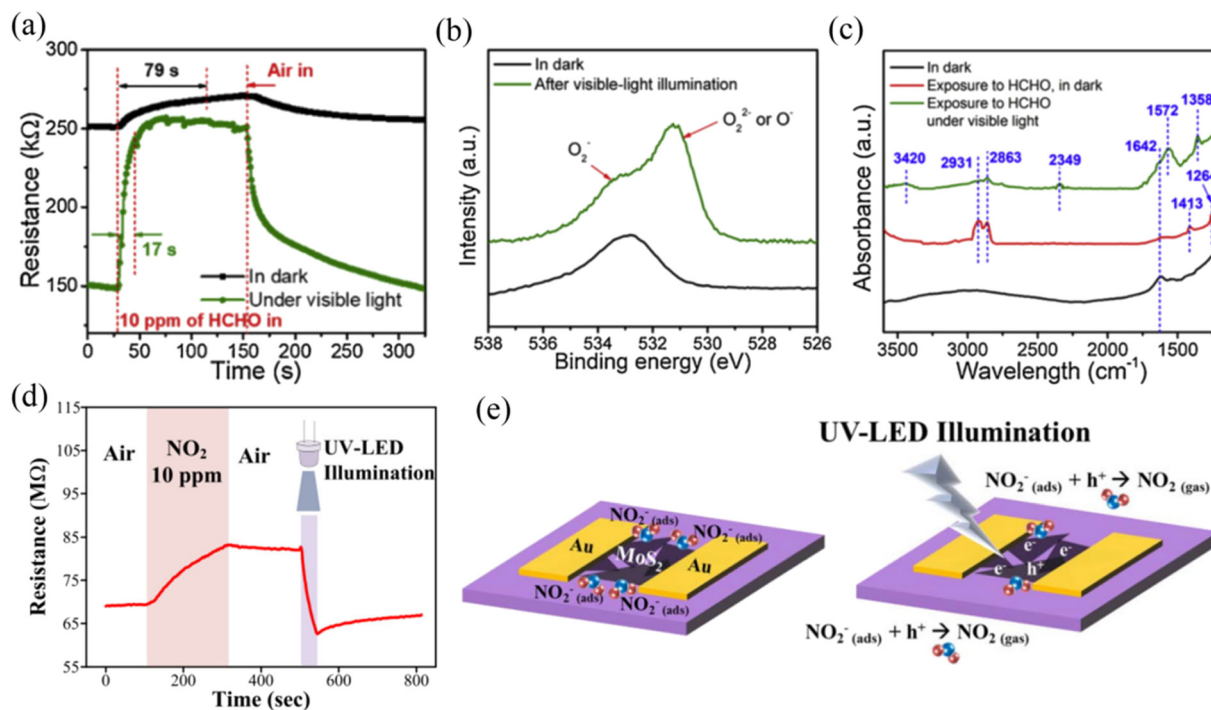


Fig. 6 (a) Dynamic resistance variations of the MoS₂/rGO sensor to 10 ppm HCHO in the dark and under visible-light illumination. (b) O 1s XPS spectra of MoS₂ in the dark and after visible-light illumination for 5 min. (c) *in situ* IR spectra of the MoS₂ sample under different conditions. Reprinted with permission from ref. 72. Copyright 2020 Elsevier B.V. (d) Transient sensor response upon exposure to 10 ppm NO₂, and a UV-LED was turned on during the recovery process. (e) Schematic of the recovery mechanism for MoS₂ under UV-LED illumination after NO₂ exposure. Reprinted with permission from ref. 73. Copyright 2019, IOP Publishing Ltd Printed in the UK.



light, which suggests that the visible-light illumination triggered the photocatalytic oxidation of HCHO to CO₂ and H₂O on the surface of MoS₂.

Kang *et al.*⁷³ reported that UV light-illuminated MoS₂ could achieve the recovery of its initial resistance when NO₂ gas was withdrawn at RT (Fig. 6d). They believed that excitons were generated in MoS₂ under UV light illumination, which could be separated into electrons and holes when an in-plane electric field of 2 kV cm⁻¹ was applied. The absorbed NO₂⁻ by capturing electrons from MoS₂ previously would react with the photo-generated holes to result in the formation of NO₂, which accelerated the desorption process (Fig. 6e). Meanwhile, the photo-generated electrons remaining in the conduction band of MoS₂ would decrease the resistance. Thus, this explains why UV-light illumination caused a rapid return to the initial resistance of the platform after releasing NO₂ gas.

2.6 Construction of composites

The construction of MoS₂-based composite gas sensors has been demonstrated to be one of the most effective methods to improve the gas sensing properties. In comparison to pure MoS₂, MoS₂ nanocomposites with well-designed architectures are more desirable. The types of composites include binary and ternary structures, which can achieve an enhancement in

gas sensing performance by making use of the merits of each component to generate synergistic effects and construct heterojunctions. The heterojunctions include n-n, n-p, and p-p types; however, MoS₂ can exhibit either a p- or n-type gas sensing response to reductive vapor depending on its annealing temperature in air.⁷⁴ The heterojunctions can effectively rectify the electron transfer at the contact surface of two materials and increase the interface barrier due to their different Fermi levels, which can significantly improve the gas sensitivity of composite sensing materials. Moreover, MoS₂-based composites accelerate the response/recovery rate of the sensor to some extent. Therefore, constructing composites of MoS₂ may be one of the most effective modification methods. Materials compounded with MoS₂ can be classified into the following categories:

(i) Metal oxide semiconductors: n-type CeO₂,⁷⁵ ZnO,⁷⁶ SnO₂,⁷⁷ WO₃,⁷⁸ In₂O₃,⁷⁹ TiO₂,⁸⁰ and MoO₃ (ref. 81) and p-type CuO,⁸² Co₃O₄,⁸³ NiO,⁸⁴ Cu₂O,⁸⁵ PANI,⁸⁶ and PPy.⁸⁷

Bai *et al.*⁸⁸ reported the preparation of a room-temperature NO₂ gas sensor based on an MoS₂/SnO₂ p-n heterojunction. MoS₂ exhibited p-type semiconductor behavior in this work, which was induced by the oxygen vacancies/defects. The MoS₂ nanoflakes were vertically grown on the SnO₂ nanotubes *via* electrospinning, and subsequent hydrothermal method, as shown in the SEM image in Fig. 7a. The optimal MoS₂@SnO₂-2 sensor (the mole ratio of Sn:Mo

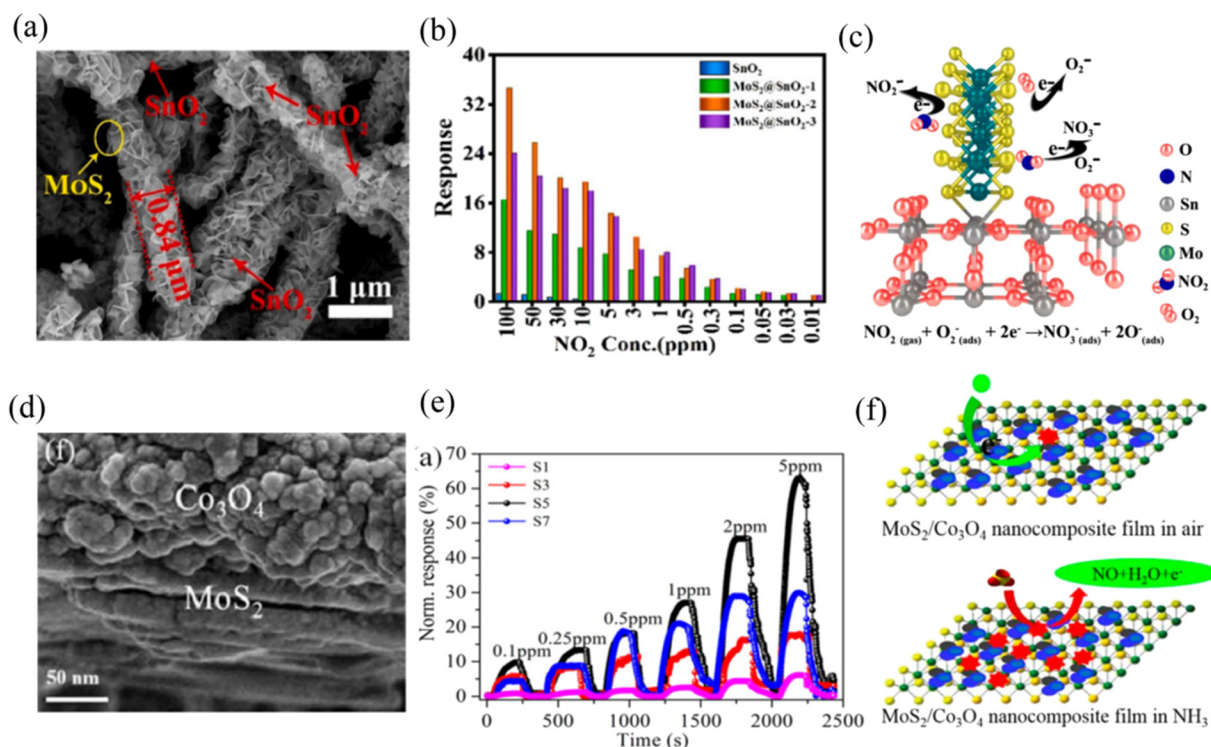


Fig. 7 (a) SEM images of MoS₂@SnO₂-2 nanocomposite. (b) Responses of the prepared sensors to different concentrations of NO₂. (c) Schematic of sensing mechanisms of MoS₂@SnO₂-2 nanocomposite. Reprinted with permission from ref. 88. Copyright 2021 Elsevier B.V. (d) SEM image of Co₃O₄/MoS₂ sample. (e) NH₃ gas-sensing properties of LbL self-assembled MoS₂/Co₃O₄ nanocomposite sensors with different layers. (f) Schematic of the sensing mechanism of n-type MoS₂/p-type Co₃O₄ hybrid in air and ammonia. Reprinted with permission from ref. 89. Copyright 2017, the American Chemical Society.



was 1:1/2) exhibited the highest sensing response value compared to the other mole ratio sensors and pristine SnO₂ sensor towards different concentrations of NO₂ gas (Fig. 7b). Meanwhile, its response/recovery times (2.2/10.54 s) were also fast. The enhancement in the gas sensing properties could be attributed to the unique morphological structure, high specific surface area, large number of sulfur edge active sites, and p-n heterojunction created between MoS₂ and SnO₂. The sensing mechanism could be explained by the surface depletion layer model caused by oxygen adsorption, as shown in Fig. 7c. The ionized chemisorbed oxygen (O₂⁻) produced on the surface of sensing material formed NO₃⁻ by introducing NO₂ gas due to the oxidation reaction. This process caused a change in the carrier concentration, and especially after the formation of heterojunctions, this change would be greater.

Zhang *et al.*⁸⁹ fabricated a Co₃O₄/MoS₂ p-n heterojunction nanocomposite (Fig. 7d) sensor on interdigital electrodes *via* the layer-by-layer self-assembly route. Firstly, they discussed the effect of the number of layers on the composite assembled with one, three, five, and seven layers (S1, S3, S5, and S7) on the NH₃ gas sensing performance at RT, respectively. The five-layered Co₃O₄/MoS₂ sensor exhibited the best NH₃ sensing response, as shown in Fig. 7e. The sensing mechanism could also be ascribed to the large change in the width of the depletion layer when exposed to an air and NH₃ atmosphere, respectively, which was caused by the p-n heterojunction. NH₃ reacted with the adsorbed O₂⁻ to produce NO gas and release electrons (Fig. 7f), which resulted in an increase in the resistance of the sensor.

(ii) Two-dimensional materials: transition metal dichalcogenides (TMDs) such as WS₂,^{90,91} WSe₂,⁹² and VS₂,⁹³ hexagonal boron nitride (h-BN);⁹⁴ transition metal carbides, nitrides and/or carbonitrides such as Ti₃C₂T_x MXene;⁹⁵ reduced graphene oxide (rGO);^{96–98} and graphene.⁹⁹

The MoS₂ composites with other TMDs can change the amplitude of variation in target gases to increase the response value. For example, Zheng *et al.*¹⁰⁰ synthesized 2D van der Waals junctions by stacking n-type and p-type atomically thin MoS₂ films *via* chemical vapor deposition (CVD) and soft-chemistry route, respectively. This idea was very interesting and meaningful. They employed the two different semiconductor characteristics of MoS₂ to construct a p-n junction sensor. This sensor displayed outstanding sensitivity to NO₂ at RT, which was much higher than that of pristine n-type and p-type MoS₂. The enhanced sensing performance was ascribed to the built-in electric field generated at the p-n interface, which resulted in a huge change in resistance upon contact with NO₂ molecules.

Ikram *et al.*⁹¹ reported the preparation of an MoS₂@WS₂ heterojunction sensor for the effective detection of NO₂ at RT. When the sensor contacted with NO₂ molecules, more electrons in the composite could be captured by NO₂ compared to that of the single MoS₂ or WS₂ component due to the double-electron supply effect, which caused a higher change in resistance. In addition, Zhang *et al.*⁹³ proposed

that the combination of different TMDs with different geometrical and electronically energetic alignments exhibited unique features. Porous VS₂ with intrinsic metallic and highly conductive characteristics was epitaxially grown on MoS₂ nanosheets. They constructed an MoS₂/VS₂ quartz crystal microbalance sensor, which showed high sensitivity and selectivity to NH₃. The metallic VS₂ transferred electrons to MoS₂, causing more electrons to accumulate on the side of MoS₂, which contributed to the O₂ acquiring a large number of electrons to form adsorbed oxygen and increased the initial resistance of the heterostructure in air. Therefore, it showed better sensitivity than the pure MoS₂ and VS₂.

Liu *et al.*⁹⁴ designed an MoS₂ gas sensor capped with a thin layer of h-BN. They found that the h-BN layer capped on the MoS₂ layer improved the device stability, robustness and anti-fading capacity, while leaving the gas sensing capability unchanged due to the strong oxidation resistance of h-BN.

In the case of Ti₃C₂T_x MXene, it has high conductivity and active termination groups of T_x = -F, -OH, and -O. Yan *et al.*¹⁰¹ analyzed the NO₂ sensing reinforcement of the MoS₂/Ti₃C₂T_x MXene composite sensor, where they considered that the excellent electrical property of MXene will make up for the deficiency of MoS₂ in this respect. A large number of carriers was transferred from MXene to MoS₂ to create a similar Fermi energy level. The role of MXene was similar to the above-mentioned metallic VS₂. In addition, the surface active groups would be more conducive to adsorbing the NO₂ oxidizing gas.

Graphene and rGO with a large surface area and high charge carrier mobility, which have been considered as alternative sensing material candidates or gas sensing performance modification materials. Graphene can be used to detect individual molecules, causing the ultimate sensitivity.¹⁰² Sangeetha *et al.*¹⁰³ reported that the enhanced gas sensing properties of an MoS₂/graphene sensor towards NO₂ including outstanding sensitivity and rapid response/recovery times (22/35 s) were attributed to the synergistic effect of the two materials. The MoS₂ nanoparticles connected with graphene promoted the absorption of more gas molecules in the presence of evanescent wave light. Compared with graphene, rGO is rich in surface vacancies and oxygen functional groups.^{104,105} Chen *et al.*⁹⁶ constructed 3D MoS₂/rGO composites *via* a low temperature self-assembly method as a low-temperature NO₂ gas sensor. They believed that the improvement in the gas sensing performance of MoS₂/rGO compared to pure MoS₂ and rGO in addition to the contribution of heterojunction between the rGO nanosheet and MoS₂ nanoflowers, was attributed to the chemically active sites, large surface area, and van der Waals forces of rGO, which are also advantageous for gas adsorption.

(iii) Other functional materials: multi-walled carbon nanotubes (MWCNT),¹⁰⁶ poly(3-hexylthiophene) (P3HT),¹⁰⁷ C₃N₄,¹⁰⁸ PbS,¹⁰⁹ GaN,¹¹⁰ CdTe,¹¹¹ ZnS,¹¹² SnS₂,¹¹³ *etc.*

MoS₂ composites with other functional materials also combine the merits of these materials such as high electrical



conductivity, unique electronic transfer channels, similar sensitivity and selectivity, and high specific surface area to comprehensively improve the gas sensing performance or use the synergistic effect between these materials and MoS₂ to achieve the goal of gas sensing. Chen *et al.*¹¹² synthesized 2D/0D MoS₂/ZnS heterostructures, which achieved the highly sensitive and recoverable detection of NO₂ at RT. The recovery time of the composite sensor to 5 ppm NO₂ was 4.6 min, which was much shorter than that of bare MoS₂. The p–n heterojunction created between MoS₂ and ZnS could act as a charge transfer bridge during NO₂ adsorption and desorption. Besides, the enriched active sites of MoS₂, the synergistic effects between the two components promoted an enhancement in sensing properties.

Jaiswal *et al.*¹¹¹ employed CdTe quantum dots with high sensitivity to NO₂ gas at RT to decorate MoS₂ nanoworms. The composite sensor could efficiently achieve spill-over effects and change the electronic structure. Furthermore, the p–n heterojunction, synergistic effect, defective intersurfaces, and unique morphology with large specific surface area jointly facilitated the high and fast adsorption of NO₂ molecules.

Besides the above-mentioned MoS₂-based binary-structured composite gas sensors, MoS₂-based ternary-structured composites have also been designed to achieve ideal gas sensing performances due to their unique/novel

multi-level hierarchical heterostructures and multiple synergistic effects.

In our previous work,¹¹⁴ a novel two-dimensional Ti₃C₂T_x MXene@TiO₂/MoS₂ heterostructure was synthesized for the efficient and selective detection of NH₃ at RT. Its morphology is shown in Fig. 8a, where MoS₂ nanosheets grew on the surface of MXene and rectangular TiO₂ particles were derived from MXene during the high-temperature hydrothermal process. It could be seen that the composite sensors (MTM) exhibited a higher NH₃ gas sensing response value compared to that of pristine MXene and MoS₂, as shown in Fig. 8b, and outstanding selectivity was exhibited by the MTM-2 composite sensor, as shown in Fig. 8c. Finally, we concluded that the enhancement in the gas sensing performance was ascribed to the unique morphology and p–n heterojunction of the ternary MXene@TiO₂/MoS₂ composite. Moreover, the insertion of TiO₂ expanded the interlayer spacing of the Ti₃-C₂T_x MXene and provided more reactive sites for NH₃ adsorption.

Ding *et al.*¹¹⁵ constructed an MoS₂-rGO-Cu₂O (MG-Cu) ternary composite for the efficient detection of NO₂ at RT. The hollow Cu₂O nanospheres were anchored on the surface of MoS₂-rGO, and the TEM image of this composite is shown in Fig. 8d. The sensor exhibited 11- and 5-times higher sensing response values to 500 ppb NO₂ compared to pure MoS₂ and binary MoS₂-rGO, respectively (Fig. 8e). Besides, it

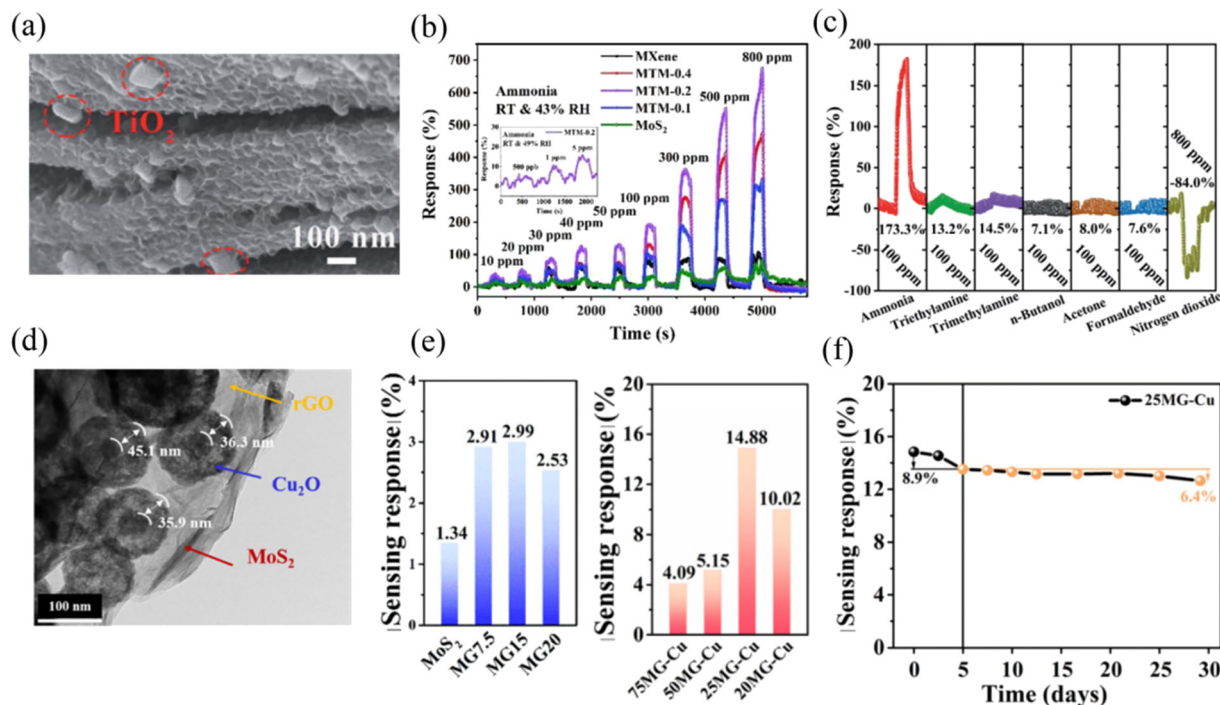


Fig. 8 (a) SEM images of Ti₃C₂T_x MXene@TiO₂/MoS₂ (MTM-0.2). (b) Dynamic sensing characteristics of the prepared sensors to ammonia vapor at RT of 27 °C and RH of 43%. (c) Gas sensing responses of the Ti₃C₂T_x MXene@TiO₂/MoS₂ (MTM-0.2)-based gas sensor for a concentration of 100 ppm of various gases at RT of 25 °C and RH of 41%. Reprinted with permission from ref. 114. Copyright 2022, The Royal Society of Chemistry. (d) TEM image of MoS₂-rGO-Cu₂O (MG-Cu) ternary composite. (e) Sensing response of MG and MG-Cu with different amounts of graphene to 500 ppb NO₂ at room temperature. (f) Stability of 25 MG-Cu sensor to 500 ppb NO₂ at room temperature. Reprinted with permission from ref. 115. Copyright 2021, Elsevier B.V.



also displayed excellent long-term stability (Fig. 8f). The superior sensing properties of this ternary composite sensor were mainly ascribed to the porous Cu₂O, which acted as a gas molecule permeation diffusion channel, while MoS₂-rGO acted as the bridge for electron transport. Meanwhile, the synergy of the shell-structure and heterojunction constructions among the three components contributed to the enhanced performance.

3. Categories of gas detected by MoS₂-based sensors

According to the discussion in the previous section, it can be seen that MoS₂-based gas sensors mainly show excellent recognition for NO₂ and NH₃ gases at RT. Alternatively, a few other gases can also be detected at RT such as nitric oxide (NO), hydrogen (H₂), ethanol, methanol, formaldehyde (HCHO), carbon monoxide (CO), sulfur dioxide (SO₂), benzene, acetone, and triethylamine (TEA), but the relevant reports are relatively scarce. In this case, it is worth exploring why MoS₂-based gas sensors can identify these gases, especially for NO₂ and NH₃ detection. In this section, we will classify the different gases detected by MoS₂-based gas sensors at RT and discuss their sensing mechanisms.

3.1 NO₂, NO, CO, and SO₂

NO₂ possesses high electrophilicity as an electron acceptor,¹¹² which means that it can easily trap electrons from the conduction band of sensing materials without high energies, causing an increase in the hole concentration of MoS₂ and a large change in the resistance of the sensor. Moreover, MoS₂ has more adsorption sites for NO₂ molecules. Regarding this, some theoretical calculation studies have verified the stronger affinity of MoS₂ for NO₂. Yue *et al.*¹¹⁶ employed first-principles calculations to investigate the adsorption energy and charge transfer of various gas molecules such as H₂, O₂, H₂O, NH₃, NO, NO₂, and CO on monolayer MoS₂. They concluded that all the calculated gas molecules were physically adsorbed on the surface of MoS₂. However, regardless of the adsorption sites on MoS₂ including H site (top of the MoS₂ hexagon), T_s (top of S atoms) site, and B site (top of Mo-S bonds), NO₂ exhibited the highest adsorption energy and more charge transfer than other gases. Meanwhile, the H site was the most favorable adsorption site for H₂O, NH₃, and NO₂ molecules, resulting in adsorption energies of -234, -250, and -276 meV, respectively. Jiang *et al.*¹¹⁷ also carried out the first-principles calculations to verify that perfect-layered MoS₂ (without vacancy) exhibited higher adsorption energies for N-based gas molecules such as NO and NO₂ compared with other gases. Meanwhile, this team also calculated the adsorption energies of NH₃, NO, and NO₂ adsorbed on defective MoS₂ with Mo vacancy and S vacancy. They found that the adsorption energies of NO and NO₂ on defective MoS₂ with Mo vacancy increased remarkably compared with

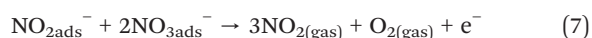
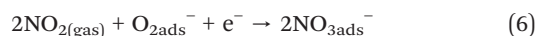
perfect MoS₂. The electron localization function indicated that O-S and N-S covalent bonds were formed between NO and defective MoS₂, NO₂ and defective MoS₂, respectively, demonstrating that there was chemical adsorption between them.

Besides theoretical studies, experimental studies have also confirmed that there is strong interaction between NO₂ molecules and MoS₂. Ikram *et al.*¹⁰⁸ reported the preparation of a highly sensitive RT NO₂ sensor based on MoS₂/C₃N₄ hybrid material. They confirmed the presence of the Mo-N bond based on the high-resolution N 1s spectra of the MoS₂/C₃N₄ hybrid after absorbing NO₂, illustrating that Mo was a strong adsorption site for N-based gases.

The gas sensing mechanism of MoS₂-based gas sensors towards NO₂ at RT is mainly based on the Langmuir-Hinshelwood (adsorption-desorption) model.^{118,119} Specifically, in an air atmosphere, the O₂ molecules surround the surface of MoS₂-based nanomaterials and extract free electrons from the conduction band of MoS₂ to form adsorbed oxygen species such as O₂⁻, O⁻, and O²⁻. The equations describing this reaction are as follows:



However, the oxygen ion O₂⁻ is predominant at low temperature (RT~150 °C).¹²⁰ The formation of O₂⁻ results in a high baseline resistance for n-type MoS₂ or low baseline resistance for p-type MoS₂. When introducing NO₂ on the surface of MoS₂, the oxidising gas further captures electrons from MoS₂ to form NO₂⁻, and more holes accumulate in the conduction band of MoS₂, causing a higher resistance for n-type MoS₂ or lower resistance for p-type MoS₂. Meanwhile, the NO₂ gas will also react with O₂⁻ to generate NO₃⁻. When an MoS₂-based sensor is put into an air atmosphere again, NO₂⁻ and NO₃⁻ would desorb and the released electrons come back to MoS₂, and thus the resistance will decrease for n-type MoS₂ or increase for p-type MoS₂ again. The reaction is as follows:



In the case of NO gas, it is also an electron acceptor and easily oxidized into NO₂ gas in air. Although some theoretical studies show that the adsorption interaction of MoS₂ for NO is weaker than that of NO₂, there is also chemical adsorption and significant charge transfer between it and MoS₂, as



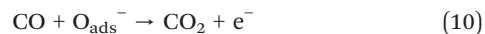
confirmed by density of states analysis.⁴⁶ To date, NO room-temperature gas sensors based on MoS₂ have also been reported, and the sensing mechanism is according to the following equations:



When MoS₂-based gas sensors are exposed to NO gas, the reduction reaction of NO occurred, as shown in eqn (8), which leads to an increase in resistance for n-type MoS₂. Once the NO gas is withdrawn, the electrons return from NO_{ads}[−] to MoS₂, resulting in a decrease in the resistance of MoS₂.

In addition to NO₂ and NO gases, CO and SO₂ can also be detected by MoS₂-based gas sensors at RT, but there are not

many reports in this regard. Their sensing mechanisms are the same as NO₂ and NO on the surface of MoS₂, which is based on the interaction between absorbing oxygen and gas molecules to release electrons, leading to a change in the resistance of MoS₂. Zhang *et al.*¹²¹ reported the preparation of a highly sensitive Ag-loaded ZnO/MoS₂ ternary nanocomposite room-temperature CO sensor. They described the sensing reaction by eqn (10), as follows:



When the sensor was exposed to CO, its resistance decreased due to the release of electrons. The presence of noble metal Ag with catalytic activity accelerated the reaction.

Zhang *et al.*¹²² demonstrated that Ni-doped MoS₂-based gas sensors exhibited an excellent SO₂ sensing performance at RT. The Ni-doped MoS₂ system had strong electrochemical

Table 1 A summary of MoS₂-based room-temperature NO₂ gas sensors

Materials	Gases	Concentration (ppm)	Response (R_a/R_g , R_g/R_a) or $[(\Delta R/R) \times 100\%]$	Response/recovery time (s)	Ref./year
MoS ₂ nanowires	NO ₂	5	~10.5%	Incomplete recovery	30/2018
Vertically aligned MoS ₂ on SiO ₂ nanorod	NO ₂	50	390%	Incomplete recovery	124/2018
MoS ₂ monolayer	NO ₂	0.02	20%	~12 h	125/2014
MoS ₂ bilayer film	NO ₂	100	26.4%	11.3/5.3 min	126/2017
MoS ₂ nanosheets	NO ₂	5	88%	85/1420	127/2021
MoS ₂ vertically aligned layers	NO ₂	100	10%	Not recovered	128/2015
Vertically aligned MoS ₂ flake	NO ₂	50	~48.32%	98/not recovered	129/2018
		1	~3.4%	68/not recovered	
MoS ₂ nanoflowers	NO ₂	5	~59%	125/485	34/2020
MoS ₂ flakes (UV light-activated)	NO ₂	100	27.92%	29/350	130/2017
MoS ₂ nanosheets (UV light-activated)	NO ₂	5	~1.15	Complete recovery	73/2019
Au/MoS ₂ (visible light-enhanced)	NO ₂	1	8.1	~27	131/2021
La/MoS ₂	NO ₂	10	45.34%	89.1/95.4	132/2020
Co/MoS ₂	NO ₂	100	51.08%	10/600	58/2022
Ni/MoS ₂	NO ₂	200	45.2%	28/250	133/2022
WO ₃ /MoS ₂	NO ₂	10	1.17	Complete recovery	78/2019
SnO ₂ /MoS ₂	NO ₂	5	18.7	74/complete recovery	77/2019
ZnO/MoS ₂	NO ₂	5	3050%	40/300	118/2018
In ₂ O ₃ /MoS ₂	NO ₂	1	39.4	72/118	79/2022
CuO/MoS ₂ (red light-activated)	NO ₂	10	~8	33.9/55.6	134/2022
MOF-In ₂ O ₃ /MoS ₂	NO ₂	10	9.36	152/179 (20 ppm)	135/2019
MoS ₂ @MoO ₂	NO ₂	100	~19	1.06/22.9	136/2019
PbS/MoS ₂	NO ₂	100	22.5%	30/235	109/2019
MoS ₂ /ZnS	NO ₂	5	7.2	~4.6 min	112/2021
CdTe/MoS ₂	NO ₂	10	~40%	16/114	111/2020
SnS ₂ /MoS ₂	NO ₂	100	~26	15.2/28.2	137/2020
WS ₂ /MoS ₂	NO ₂	0.02	26.12	1.6/27.7	91/2019
MoS ₂ /Ti ₃ C ₂ T _x MXene	NO ₂	100	65.6%	About 750/not recovered	101/2022
Ti ₃ C ₂ /MoS ₂	NO ₂	100	46.9	Incomplete recovery	95/2022
CTAB-MoS ₂ /rGO	NO ₂	8	37.64%	Incomplete recovery	97/2022
Mo ₂ Ti ₃ C ₂ T _x /MoS ₂	NO ₂	50	415.8%	34.8/140.5	138/2022
MoS ₂ /C ₃ N ₄	NO ₂	30	~49	2.3/30.5	108/2020
MoS ₂ -rGO-Cu ₂ O	NO ₂	0.5	14.8%	Incomplete recovery	115/2021
rGO/MoS ₂	NO ₂	40	25	160/3300	139/2018
MoS _{2-x} Se _x	NO	3	48%	410/340	140/2021
3D cone-shaped MoS ₂ (UV light-activated)	NO	0.06	200%	130/~	68/2019
3D cone-shaped MoS ₂ (white light-activated)	NO	0.06	75%	150/~	68/2019
MoS ₂ monolayer (UV light-activated)	NO	100	25.63%	About 250/600	141/2019
CNFs/CoS ₂ /MoS ₂	NO	50	19%	60/260 min	142/2020
MoS ₂ /Si nanowire array	NO	50	3518%	680/668	143/2017
Pt-ZnO/MoS ₂	CO	5	5.08%	45/60	121/2017
Ni-MoS ₂	SO ₂	5	7.4%	50/56	122/2017
SnO ₂ /MoS ₂ (UV light-activated)	SO ₂	1	4.68	217/633	144/2021



activity due to the overlap of the conduction band and valence band, where the flow of electrons was easier from the valence band to conduction band. When the SO₂ and Ni-doped MoS₂ system interacted, the bond length values of the SO₂ molecules and the electronic structure of the Ni-doped MoS₂ system changed significantly, as verified by DFT calculation.

The sensing mechanism of MoS₂-based gas sensors towards SO₂ is based on eqn (11),¹²³ as follows:

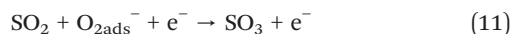


Table 1 summarizes the MoS₂ nanomaterial-based gas sensors for the detection of NO₂, NO, CO, and SO₂ gases at RT in recent years. It can be seen that there are more reports focused on the detection of NO₂ rather than NO, CO, and SO₂, illustrating that MoS₂ has a strong interaction for N-based gases. In addition, it is difficult for pristine MoS₂ NO₂ sensors to recovery completely, and thus several modification strategies have greatly improved their response and recovery rate to a certain extent.

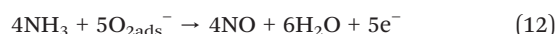
3.2 NH₃

In contrast to NO₂, NH₃ gas is a well-known electron donor owing to the fact that it contains a pair of lone electrons, which are not involved in bonding. Therefore, the electron concentration will increase for the n-type MoS₂ sensing layer when exposed to NH₃, resulting in a low resistance. The adsorption energies of CO, NO₂, and NH₃ on pristine MoS₂ were analyzed by DFT calculation.¹⁴⁵ The results showed that the most stable adsorption energies for CO, NO₂, and NH₃ were 0.008, −0.131, and −0.217 eV, respectively, implying that the high interaction between NH₃ and MoS₂. The low positive value of 0.008 indicated that CO on MoS₂ was exothermic, unstable, and weakly adsorbed. Zhao *et al.*¹⁴⁶ also employed

DFT calculation to investigate the adsorption energies of O₂, NO, NO₂, and NH₃ gas molecules on pristine MoS₂. They found that the adsorption energies values of O₂, NO, NO₂, and NH₃ gases on MoS₂ were 0.013, 0.026, 0.037, and 0.041 eV, respectively. Although all these gases exhibited weak physical adsorption interaction on MoS₂, obviously, NH₃ had the highest.

Sharma *et al.*¹⁴⁷ and Singh *et al.*¹⁴⁸ verified the high sensitivity of MoS₂ to NH₃ gas at RT *via* experimental measurements. Another important parameter involved is the response/recovery time, and these researchers observed that the pristine MoS₂-based NH₃ sensors showed a fast response/recovery time of 22/32 s towards 100 ppm NH₃ and 75/130 s towards 50 ppm NH₃, indicating that a fast and complete recovery can be achieved when NH₃ gas was detected.

The gas sensing mechanism of the MoS₂-based gas sensor towards NH₃ at RT is also based on the adsorption-desorption theory. The following equations are used to describe the interaction between NH₃ and the MoS₂ sensing layer.



When MoS₂ sensors are exposed to the reducing NH₃ gas, the NH₃ molecules will react with O_{2ads}[−] to form NO and H₂O accompanied by the release of electrons; meanwhile, NH₃ molecule itself contains lone pair electrons, which makes more electrons return to the conduction band of MoS₂, causing a large change in resistance.

To further improve the gas sensing performance of MoS₂-based gas sensors to NH₃ at RT, several MoS₂ nanocomposite NH₃ gas sensors have been proposed in recent years. Table 2 presents a summary of MoS₂ nanomaterial-based gas sensors for the detection of NH₃ gas at RT.

Table 2 A summary of MoS₂-based room-temperature NH₃ gas sensors

Materials	Concentration (ppm)	Response (R_a/R_g , R_g/R_a) or $[(\Delta R/R) \times 100\%]$	Response/recovery time (s)	Ref./year
NiO/MoS ₂	10	63%	160/117 (20 ppm)	84/2019
MoS ₂ /CuO	100	~47%	17/26	82/2018
MoS ₂ nanostructure	50	10%	75/130	148/2020
MoS ₂ thin film	100	2.2	22/32	137/2018
MoS ₂ /ZnO	50	46.2%	10/11	149/2017
MoS ₂ /Co ₃ O ₄	5	~65%	98/100	89/2017
MoS ₂ /MWCNTs	100	~42%	80/90 (50 ppm)	106/2021
SnO ₂ /MoS ₂	50	91.26	23/1.6	33/2020
MoS ₂ /MWCNT	150	~26%	65/70	150/2020
Co ₃ O ₄ /MoS ₂	50	4.2	105/353	83/2022
MoS ₂ /SnO ₂	50	53%	Complete recovery	151/2021
PANI/MoS ₂ /SnO ₂	100	10.9	21/130	152/2021
MoS ₂ nanochains	200	40%	80/70	153/2022
P3HT/MoS ₂	4	8%	100/500	107/2016
MoS ₂ /MoO ₃	50	~54%	45/53	154/2021
PANI/MWCNTs/MoS ₂	5	40.12%	56/50	155/2018
PANI/MoS ₂	5	10.94%	98/57	155/2018
Ti ₃ C ₂ T _x MXene@TiO ₂ /MoS ₂	100	163.3%	117/88	114/2022

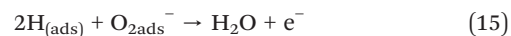


3.3 H₂

H₂ as an abundant, green and renewable energy source has been used in various fields such as fuel cells, automobiles, and power plants.¹⁵⁶ Moreover, it is also applied in the chemical industry, nuclear reactors, petroleum extraction, and semiconductor processing.¹⁵⁷ However, H₂ is also associated with many potential safety hazards due to its explosive and flammable nature.¹⁵⁸ Especially when its concentration is higher than 4% in the atmosphere, an explosion will occur. Therefore, the efficient detection of H₂ is particularly important. Currently, although SMO H₂ sensors exhibit high gas sensing response values, their high operating temperature also brings hidden dangers to a certain extent because the explosive limit of H₂ is easily reached at a high temperature. Thus, the detection of H₂ at low or room temperature will greatly improve the safety. To date, many low or room-temperature H₂ sensors based on MoS₂ have been reported. Theoretically, MoS₂ is not sensitive to nonpolar molecules of H₂.¹⁵⁹ Bollinger *et al.*¹⁶⁰ believed that the edges of MoS₂ behave like metallic inter-connecting wires for the adsorption of H₂ at RT. Dolui *et al.*¹⁶¹ and Gomez *et al.*¹⁶² also proposed that H₂ behaves as an electron acceptor, which is favourable for absorption along the edges of MoS₂ flakes. To date, the main approach employed to increase the sensitivity of MoS₂ to H₂ is its functionalization with noble metals including Au, Ag, Pt, and Pd. Zhang *et al.*¹⁶³ investigated the effect of different noble metals (Cu, Au, Ag, Pt, and Pd) decorated on monolayer MoS₂ on its hydrogen sensing performances by first principles. They concluded that the introduction of all the noble metals had a positive effect on H₂ adsorption, which contributed to the hybridization of the noble metal d, S p, Mo d and H s orbitals. Especially Pt and Pd could enhance the adsorption interaction and increase the charge transfer between H₂ molecules and monolayer MoS₂. Some experimental studies are also consistent with the theoretical results. Baek *et al.*,¹⁶⁴ Jaiswal *et al.*⁴⁹ and Mai *et al.*¹⁶⁵ used Pd to functionalize MoS₂ and realize the detection of H₂ at RT. The former

research groups suggested that the mechanism of H₂ sensing on Pd/MoS₂ is ascribed to the electron transfer from MoS₂ and Pd in air due to the lower work function of MoS₂ than Pd. Alternatively, the formation of Pd-hydride (PdHx) on Pd surface when exposed to H₂ resulted in electron transfer in the opposite direction from PdHx to MoS₂, resulting in a change in sensor resistance. The latter research group concluded that the deposition of Pd nanoclusters on MoS₂ caused p-type semiconductor behavior in the Pd/MoS₂ composite. Meanwhile, the strong affinity of Pd provided more favorable adsorption sites for H₂ molecules and initiated their chemical reactions.

Besides the use of noble metals to trigger the sensitive response of MoS₂ to H₂ at RT, another strategy is to compound some potential materials that respond to H₂, such as MoO₃,¹⁶⁶ graphene,¹⁶⁷ and SnO₂ (ref. 168) with MoS₂ as suitable templates or supports. Table 3 displays the MoS₂ nanomaterial-based gas sensors for H₂ gas detection at RT. The sensing mechanism can be explained based on the interaction between H₂ molecules and O_{2ads}⁻. The whole reaction can be given by the following equations:



3.4 Other VOCs

The other VOC gases that can be detected by MoS₂-based gas sensors at RT include ethanol, methanol, formaldehyde (HCHO), and benzene. VOCs gases, as reducing agents, present electron-donating characteristics similar to NH₃. To date, there are a few reports on the detection of these gases at RT by MoS₂-based sensing devices, which mainly consider the activity, electronic characteristics, molecular size of the

Table 3 A summary of MoS₂-based room-temperature H₂ gas sensors

Materials	Concentration (ppm)	Response (R_a/R_g , R_g/R_a) or $[(\Delta R/R) \times 100\%]$	Response/recovery time (s)	Ref./year
MoS ₂ /Cs _x WO ₃	500	50.6%	60/120	169/2022
UNCD/MoS ₂ /ZnO	100	50.3%	8/12	170/2019
Bulk-MoS ₂	100	14.2%	28/42	171/2019
Pd-MoS ₂ /Si	1%	~53.3%	~13.1/15.03 min	164/2017
RGO/MoS ₂	200	~1.1%	~	172/2017
Pd-SnO ₂ /MoS ₂	5000	18%	30/19	173/2017
Pd/MoS ₂ (light-activated)	140	17.45 ± 1.02%	351/515 (120 ppm)	165/2021
Pd/MoS ₂	500	33.7%	16/38	49/2020
Vertically aligned MoS ₂ /Si	100	685.7%	109/102	174/2016
Edge-oriented MoS ₂ flake	10 000	1%	14.3/137	175/2017
MoS ₂ /GaN	5%	~25%	~	110/2019
Zn-doped MoO ₃ /MoS ₂	500	28.91%	24.6/18.5	176/2022
MoS ₂ /graphene	1000	8.1%	32/33	177/2022
MoS ₂ /ZnO	500	51.5%	14/19	178/2021



Table 4 A summary of MoS₂-based room-temperature ethanol, methanol, formaldehyde, and benzene gas sensors

Materials	Gases	Concentration (ppm)	Response (R_a/R_g , R_g/R_a) or $[(\Delta R/R) \times 100\%]$	Response/recovery time (s)	Ref./year
CeO ₂ /MoS ₂	Ethanol	50	7.78	7/5	75/2021
α -Fe ₂ O ₃ /MoS ₂	Ethanol	100	88.9%	6/5 (30 ppm)	183/2018
Fe-TiO ₂ /MoS ₂	Ethanol	5	150%	62/49 (1 ppm)	179/2018
Ag/MoS ₂	Methanol	100	21.6%	240/1100	50/2021
In ₂ O ₃ /MoS ₂	Formaldehyde	50	75.2%	14/22	185/2018
rGO/MoS ₂	Formaldehyde	10	~2.7%	73/~	184/2017
rGO/MoS ₂	Formaldehyde	10	4.8%	~	186/2017
rGO/MoS ₂ (visible-light activated)	Formaldehyde	10	64%	79/17	72/2021
Pd-TiO ₂ /MoS ₂	Benzene	50	64%	13/10	182/2018

gas itself, and the affinity of sensitive materials to gas molecules.

Wu *et al.*¹⁷⁹ prepared an Fe-TiO₂/MoS₂ composite film ethanol RT sensor. They proposed that Fe ion doping can optimize the electrical property of the sensing material. The sensor was sensitive to ethanol, which was attributed to the fact that the hydroxyl in the rotating ethanol molecule faced the Fe-TiO₂ substrate and elongation of the C-O and H-O bonds on the adsorption surface of Fe-TiO₂, which resulted in a shorter adsorption distance and higher adsorption strength. The density of states revealed that there was strong adsorption interaction between ethanol and Fe-TiO₂ due to the large shift in the energy level of the Fe 3d and O 2p orbitals after adsorption. Finally, combined with the p-n heterojunctions generated at the interface of n-type Fe-TiO₂ and p-type MoS₂, the sensing response to ethanol was stronger.

Chakraborty *et al.*¹⁸⁰ analyzed the highly selective methanol sensing mechanism of electrodeposited pristine MoS₂ using first principle analysis. They found that although the electron-donating capability and charge transfer of 2-propanol and ethanol were higher than that of methanol, the smaller dimension of methanol, two favorable adsorption sites (Ori-A and Ori-B) of methanol on MoS₂ surface, and approximately 20-times larger adsorption energy than that of ethanol and 2-propanol were the main reasons for the high sensitivity of MoS₂ towards the detection of methanol.

Actually, pristine MoS₂ does not have good sensitivity to formaldehyde, although it is a small molecule. Deng *et al.*¹⁸¹ employed DFT to investigate the adsorption of formaldehyde on Ni-, Pt-, Ti- and Pd-doped monolayer MoS₂, respectively. They found that Ti-MoS₂ was the dominant one in terms of adsorption energy. Moreover, the projected density of states (PDOS) and charge transfer indicate that the interaction between the formaldehyde molecule and Ti dopant was chemisorption *via* the Ti-O bond, illustrating that Ti-MoS₂ may be suitable for the detection of formaldehyde. In addition, some compounds based on MoS₂ can also be sensitive to formaldehyde, but the mechanism of their sensitivity has not been clearly defined.

Zhang *et al.*¹⁸² reported that a Pd-TiO₂/MoS₂ composite sensor showed selectivity and sensitivity towards benzene at RT. The sensing mechanism could be ascribed to the fact

that Pd in TiO₂/MoS₂ has catalytic interaction toward benzene with a C-H bond and the synergistic effect of the ternary nanostructures, which can facilitate effective charge transport.

The following equations describe the reactions between the oxygen ion O₂⁻ created on the surface of MoS₂-based sensing materials and ethanol, methanol, formaldehyde, and benzene molecules, respectively.^{183,184}

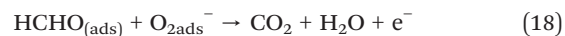


Table 4 presents a summary of the MoS₂ nanomaterial-based gas sensors for the detection of ethanol, methanol, formaldehyde, and benzene gases at RT.

4. Conclusions and outlook

Obviously, MoS₂ exhibits great capabilities in the field of gas sensing, especially for room-temperature gas detection. In this review, firstly, the strategies for improving the gas sensing performance of MoS₂ were introduced. Subsequently, the different types of gases that can be detected by MoS₂-based gas sensors at room temperature were proposed and classified. Meanwhile, the sensing mechanisms of MoS₂-based gas sensors towards different gases were also analyzed.

Pristine MoS₂ gas sensors exhibit low gas sensing response values and incomplete recovery problems at room temperature, which are unfavorable for gas detection. Consequently, various strategies have been developed for improving the gas sensing performance of MoS₂ based gas sensors including morphology design, creating sulfur vacancies, decorating with noble metals, doping elements, light assistance, and construction of composites. Although the morphology design of MoS₂ involves multiple patterns such as quantum dots, nanowires, nanosheets, and nanoflowers, each morphology exhibits unique physical and chemical properties and gas sensing performance



characteristics, and the key issue of incomplete recovery has not been well solved. The vacancies in MoS₂ belong to high energy binding sites, especially S vacancies as active sites to enhance the gas molecules adsorption. However, this high adsorption capacity will also result in a slow response and recovery rate. The decoration of the surface of MoS₂ with noble metals can assist in overcoming the problem of selectivity to a certain extent due to the fact that noble metals possess affinity for some specific gas molecules. Element doping can address the challenge of sluggish sensing of MoS₂ at room temperature owing to the adjustable active sites and electrical property. To date, doping strategies focus on theoretical calculations based on density functional theory, while experimental studies are rare. The light-assisted strategies include UV-light and visible-light activation. The power of these two lights is different, resulting in optoelectronic and photocatalytic gas sensing mechanisms, respectively, which accelerates the chemisorption reaction and causes a large change in the resistance of the sensor upon exposure to gases. Room-temperature MoS₂ nanocomposite gas sensors are the most studied at present. The construction of composites of MoS₂ (binary or ternary) can be considered one of the most effective modification methods to address the low gas sensing response and delayed recovery time of pristine MoS₂ gas sensors. The heterojunctions and synergistic effects created by the different components are conducive to improve their comprehensive gas sensing performance. Especially the high electrical conductivity, unique electronic transfer channels, and similar sensitive selectivity are observed in nanocomposites.

According to the reports on the detection of several gases by MoS₂-based gas sensors at room temperature such as NO₂, NO, SO₂, CO, NH₃, H₂, ethanol, methanol, formaldehyde, and benzene, MoS₂ seems show strong adsorption interaction for N-based gases such as NO₂ and NH₃. NO₂ as an electron acceptor exhibits high electrophilicity, which can easily trap electrons from the conduction band of MoS₂. In contrast to NO₂, NH₃ acts as an electron donor with a pair of lone electrons that can give more electrons to MoS₂, and thus the resistance of MoS₂ sensors change greatly. Besides NO₂ and NH₃, H₂ can also be detected by MoS₂-based gas sensors at room temperature. Several researchers have proposed that H₂ in nature favor absorption along the edges of MoS₂, which behave like metallic inter-connecting wires to attract H₂ at RT. The detection of other VOC gases such as ethanol, methanol, formaldehyde, and benzene by MoS₂ nanocomposite gas sensors has also been reported, which is mainly related to the strong force on these gases at one of the special adsorption sites in the composites. To date, the sensing mechanisms of MoS₂-based gas sensors for the above-mentioned gases are mainly based on the adsorption/desorption theories. The target gases react with the adsorbed oxygen ions O_{2ads}⁻ and release electrons to the conduction band of MoS₂, resulting in a change in resistance and sensitive response.

Although the above-mentioned strategies have made great progress to improve the gas sensing properties of MoS₂-based gas sensors at room temperature, there are still some interesting research directions and challenges that deserve to be explored.

Firstly, besides the strong interaction between MoS₂ and gas molecules, the deeper reasons for the slow or incomplete recovery of MoS₂ sensors to gases need to be investigated. The transduction mechanism, intrinsic characteristics, and desorption reaction seem to affect the recovery rate. In addition, NH₃ is more easily desorbed from the surface of MoS₂ than NO₂ in the case of the same N-based gases, which is worth further discussion. Secondly, the gas sensing response, selectivity, and long-term stability of MoS₂-based gas sensors are still unsatisfactory. Therefore, novel MoS₂-based room temperature gas sensors should receive more attention. Some strategies such as adjusting the active sites of MoS₂ from basal plane to edges, constructing advanced structured MoS₂ nanocomposites, and optimizing the fabrication process of devices may be interesting points. Finally, the gas sensing mechanisms of MoS₂ materials not only depend on the theories of adsorption-desorption and charge carrier transport, where the whole reactive process is complicated, and thus more crucial interactions between MoS₂ and gas molecules need to be further studied.

Conflicts of interest

There are no conflicts to declare.

Acknowledgements

This work was supported by the National Natural Science Foundation of China (No. 41876055 and 61761047), the Yunnan Provincial Department of Science and Technology through the Key Project for the Science and Technology (Grant No. 2017FA025), Program for Innovative Research Team (in Science and Technology) in University of Yunnan Province, and Project of the Department of Education of Yunnan Province (2022Y003).

References

- 1 Y. Zhou, X. Li, Y. J. Wang, H. L. Tai and Y. C. Guo, *Anal. Chem.*, 2019, **91**, 3311–3318.
- 2 T. Jarvinen, G. S. Lorite, J. Perantie, G. Toth, S. Saarakkala, V. K. Virtanen and K. Kordas, *Nanotechnology*, 2019, **30**, 405501.
- 3 Y. J. Wang, Y. Zhou, Y. H. Wang, R. J. Zhang, J. Li, X. Li and Z. G. Zang, *Sens. Actuators, B*, 2021, **349**, 130770.
- 4 M. Sajjad and P. Feng, *Mater. Res. Bull.*, 2014, **49**, 35–38.
- 5 Y. Zhou, Y. H. Wang, Y. J. Wang, H. C. Yu, R. J. Zhang, J. Li, Z. G. Zang and X. Li, *ACS Appl. Mater. Interfaces*, 2021, **13**, 56485–56497.
- 6 M. Barzegar and B. Tudu, *Surf. Innovations*, 2018, **6**, 205–230.



- 7 Q. Li, J. P. Meng and Z. Li, *J. Mater. Chem. A*, 2022, **10**, 8107–8128.
- 8 X. H. Liu, T. T. Ma, N. Pinna and J. Zhang, *Adv. Funct. Mater.*, 2017, **27**, 1702168.
- 9 T. H. Kim, Y. H. Kim, S. Y. Park and H. W. Jang, *Chemosensors*, 2017, **5**, 15.
- 10 G. Neri, *Chemosensors*, 2017, **5**, 21.
- 11 R. Kumar, N. Goel, M. Hojamberdiev and M. Kumar, *Sens. Actuators, A*, 2020, **303**, 111875.
- 12 K. F. Mak, C. Lee, J. Hone, J. Shan and T. F. Heinz, *Phys. Rev. Lett.*, 2010, **105**, 136805.
- 13 G. C. Lu, X. H. Liu, W. Zheng, J. Y. Xie, Z. S. Li, C. M. Lou, G. L. Lei and J. Zhang, *Rare Met.*, 2022, **41**(5), 1520–1528.
- 14 Y. S. Xu, J. Y. Xie, Y. F. Zhang, F. H. Tian, C. Yang, W. Zheng, X. H. Liu, J. Zhang and N. Pinna, *J. Hazard. Mater.*, 2021, **411**, 125120.
- 15 A. V. Agrawal, R. Kumar, S. Venkatesan, A. Zakhidov, G. Yang, J. M. Bao, M. Kumar and M. Kumar, *ACS Sens.*, 2018, **3**, 998–1004.
- 16 C. Yang, J. Y. Xie, C. M. Lou, W. Zheng, X. H. Liu and J. Zhang, *Sens. Actuators, B*, 2021, **333**, 129571.
- 17 M. Kumar, A. V. Agrawal, M. Moradi and R. Yousefi, *Nanomater. Air Rem.*, 2020, 107–130, DOI: [10.1016/B978-0-12-818821-7.00006-3](https://doi.org/10.1016/B978-0-12-818821-7.00006-3).
- 18 A. V. Agrawal, N. Kumar and M. Kumar, *Nano-Micro Lett.*, 2021, **13**, 305–362.
- 19 Q. Y. He, Z. Y. Zeng, Z. Y. Yin, H. Li, S. X. Wu, X. Huang and H. Zhang, *Small*, 2012, **8**, 2994–2999.
- 20 S. M. Cui, Z. H. Wen, X. K. Huang, J. B. Chang and J. H. Chen, *Small*, 2015, **11**, 2305–2313.
- 21 B. Radisavljevic, A. Radenovic, J. Brivio, V. Giacometti and A. Kis, *Nat. Nanotechnol.*, 2011, **6**, 147–150.
- 22 K. Y. Ko, J. G. Song, Y. Kim, T. Choi, S. Shin and C. W. Lee, *ACS Nano*, 2016, **10**, 9287–9296.
- 23 M. Kan, J. Y. Wang, X. W. Li, S. H. Zhang, Y. W. Li, Y. Kawazoe, Q. Sun and P. Jena, *J. Phys. Chem. C*, 2014, **118**, 1515–1522.
- 24 D. Voiry, A. Mohiteb and M. Chhowalla, *Chem. Soc. Rev.*, 2015, **44**, 2702–2712.
- 25 R. Kumar, W. Zheng, X. H. Liu, J. Zhang and M. Kumar, *Adv. Mater. Technol.*, 2020, **5**, 1901062.
- 26 W. Zheng, X. H. Liu, J. Y. Xie, G. C. Lu and J. Zhang, *Coord. Chem. Rev.*, 2021, **447**, 214151.
- 27 A. Hermawan, N. L. W. Septiani, A. Taufik, B. Yulianto, Suyatman and S. Yin, *Nano-Micro Lett.*, 2021, **13**, 207.
- 28 Z. X. Gan, L. Z. Liu, H. Y. Wu, Y. L. Hao, Y. Shan, X. L. Wu and P. K. Chu, *Appl. Phys. Lett.*, 2015, **106**, 233113.
- 29 Y. Niu, W. C. Jiao, R. G. Wang, G. M. Ding and Y. F. Huang, *J. Mater. Chem. A*, 2016, **4**, 8198–8203.
- 30 R. Kumar, N. Goel and M. Kumar, *Appl. Phys. Lett.*, 2018, **112**, 053502.
- 31 D. J. Late, Y. K. Huang, B. Liu, J. Acharya, S. N. Shirodkar, J. J. Luo, A. M. Yan, D. Charles, U. V. Waghmare and V. P. Dravid, *ACS Nano*, 2013, **7**, 4879–4891.
- 32 W. L. Li, Y. Zhang, X. Long, J. X. Cao, X. Xin, X. X. Guan, J. F. Peng and X. J. Zheng, *Sensors*, 2019, **19**, 2123.
- 33 W. X. Wang, Y. H. Zhen, J. Y. Zhang, Y. D. Li, H. Zhong, Z. L. Jia, Y. Xiong, Q. Z. Xue, Y. G. Yan and N. S. Alharbi, *Sens. Actuators, B*, 2020, **321**, 128471.
- 34 N. T. Thang, L. T. Hong, T. H. Nguyen, C. M. Hung, N. V. Duy, N. V. Hieu and N. D. Hoa, *RSC Adv.*, 2020, **10**, 12759–12771.
- 35 H. Long, A. Harley-Trochimczyk, T. Pham, Z. Tang, T. Shi, A. Zettl, C. Carraro, M. A. Worsley and R. Maboudian, *Adv. Funct. Mater.*, 2016, **26**, 5158–5165.
- 36 J. H. Hong, Z. X. Hu, M. Probert, K. Li, D. H. Lv, X. N. Yang, L. Gu, N. N. Mao, Q. L. Feng and L. M. Xie, *Nat. Commun.*, 2015, **6**, 6293.
- 37 H. Y. Nan, Z. L. Wang, W. H. Wang, Z. Liang, Y. Lu, Q. Chen, D. W. He, P. H. Tan, F. Miao and X. R. Wang, *ACS Nano*, 2014, **8**, 5738–5745.
- 38 Z. Y. Qin, K. Xu, H. C. Yue, H. Wang, J. Zhang, C. Ouyang, C. S. Xie and D. W. Zeng, *Sens. Actuators, B*, 2018, **262**, 771–779.
- 39 D. Burman, R. Ghosh, S. Santra, S. K. Ray and P. K. Guha, *Nanotechnology*, 2017, **28**, 435502.
- 40 R. Kumar, N. Goel, A. V. Agrawal, R. Raliya, S. Rajamani, G. Gupta, P. Biswas, M. Kumar and M. Kumar, *IEEE Sens. J.*, 2020, **19**, 10214–10220.
- 41 H. X. Li, M. Huang and G. Y. Cao, *Phys. Chem. Chem. Phys.*, 2016, **21**, 15110–15117.
- 42 X. W. Chen, J. Shi, T. Wang, S. Y. Zheng, W. Lv, X. Y. Chen, J. H. Yang, M. Zeng, N. T. Hu and Y. J. Su, *ACS Sens.*, 2022, **7**, 816–826.
- 43 Y. Xia, C. Y. Hu, S. H. Guo, L. B. Zhang, M. J. Wang, J. H. Peng, L. Xu and J. Wang, *ACS Appl. Nano Mater.*, 2020, **3**, 665–673.
- 44 H. P. Komsa, J. Kotakoski, S. Kurasch, O. Lehtinen, U. Kaiser and A. V. Krasheninnikov, *Phys. Rev. Lett.*, 2012, **109**, 035503.
- 45 L. C. Zhang, Y. Y. Liang, L. M. Yu, H. J. Wang and M. L. Yin, *Sens. Actuators, B*, 2022, **359**, 131539.
- 46 F. F. Li and C. M. Shi, *Appl. Surf. Sci.*, 2018, **434**, 294–306.
- 47 X. Tian, X. X. Cui, T. R. Lai, J. R. Z. C. Yang, M. J. Xiao, B. S. Wang, X. C. Xiao and Y. D. Wang, *Nano Mater. Sci.*, 2021, **3**, 390–403.
- 48 N. Sakhuja, A. Gupta, R. Jha and N. Bhat, *J. Alloys Compd.*, 2022, **899**, 163166.
- 49 J. Jaiswal, P. Tiwari, P. Singh and R. Chandra, *Sens. Actuators, B*, 2020, **325**, 128800.
- 50 P. Halvaei, S. Dehghani and M. Mohammadzadeh, *IEEE Sens. J.*, 2021, **21**, 4233–4240.
- 51 J. Park, J. H. Mun, J. S. Shin and S. W. Kang, *R. Soc. Open Sci.*, 2019, **5**, 181462.
- 52 H. Peng, J. Lu, C. X. Wu, Z. X. Yang, H. Chen, W. J. Song, P. Q. Li and H. Z. Yin, *Appl. Surf. Sci.*, 2015, **353**, 1003–1012.
- 53 C. Liu, Y. Zhang, J. Y. Hu, J. X. Ren, Y. Q. Song, J. F. Peng, M. Ma and J. J. Tan, *Mater. Lett.*, 2020, **273**, 127961.
- 54 S. G. Ramaraj, S. Nundy, P. Zhao, D. Elamran, A. A. Tahir, Y. Hayakawa, M. Muruganathan, H. Mizuta and S. W. Kim, *ACS Omega*, 2022, **7**, 10492–10501.



- 55 Z. Xiao, W. Wu, X. W. Wu and Y. F. Zhang, *Chem. Phys. Lett.*, 2020, **755**, 137768.
- 56 W. J. Hou, H. W. Mi, R. C. Peng, S. D. Peng, W. Zeng and Q. Zhou, *Nanomaterials*, 2021, **11**, 314.
- 57 R. Y. Zhang, D. Fu, J. M. Ni, C. B. Sun and S. X. Song, *Chem. Phys. Lett.*, 2019, **715**, 273–277.
- 58 P. Bharathi, S. Harish, M. Shimomura, S. Ponnusamy, M. K. Mohan, J. Archana and M. Navaneethan, *Sens. Actuators, B*, 2022, **360**, 131600.
- 59 R. Z. Wu, J. Y. Hao, S. L. Zheng, Q. Sun, T. T. Wang, D. Zhang, H. Zhang, Y. Wang and X. Zhou, *Appl. Surf. Sci.*, 2021, **571**, 151162.
- 60 T. E. Gber, H. Louis, A. E. Owen, B. E. Etinwa, I. Benjamin, F. C. Asogwa, M. M. Orosun and E. A. Eno, *RSC Adv.*, 2022, **12**, 25992–26010.
- 61 A. Kazemi, M. Rodner, M. R. Fadavieslam, P. D. Kaushik, I. G. Ivanov, J. Eriksson, M. Syvajarvi, R. Yakimova and G. R. Yazdi, *Surf. Interfaces*, 2021, **25**, 101200.
- 62 J. Zhu, H. Zhang, Y. W. Tong, L. Zhao, Y. F. Zhang, Y. Z. Qiu and X. N. Lin, *Appl. Surf. Sci.*, 2017, **419**, 522–530.
- 63 E. Salih and A. I. Ayesh, *Phys. E*, 2021, **131**, 114736.
- 64 K. N. Ding, Y. H. Lin and M. Y. Huang, *Vacuum*, 2016, **130**, 146–153.
- 65 M. J. Szary, *Appl. Surf. Sci.*, 2021, **547**, 149026.
- 66 Y. Zhou, C. Zou, X. G. Lin and Y. C. Guo, *Appl. Phys. Lett.*, 2018, **113**, 082103.
- 67 J. Guo, R. M. Wen, J. Y. Zhai and Z. L. Wang, *Sci. Bull.*, 2019, **64**, 128–135.
- 68 Y. Z. Chen, S. W. Wang, C. C. Yang, C. H. Chung, Y. C. Wang, S. W. H. Chen, C. W. Chen, T. Y. Su, H. N. Lin, H. C. Kuo and Y. L. Chueh, *Nanoscale*, 2019, **11**, 10410–10419.
- 69 T. Pham, G. Li, E. Bekyarova, M. E. Itkis and A. Mulchandani, *ACS Nano*, 2019, **13**, 3196–3205.
- 70 P. C. Chen, S. Sukcharoenchoke, K. Ryu, L. G. Arco, A. Badmaev, C. Wang and C. Zhou, *Adv. Mater.*, 2010, **22**, 1900.
- 71 D. L. Wang, A. T. Chen and A. K. Y. Jen, *Phys. Chem. Chem. Phys.*, 2013, **15**, 5017–5021.
- 72 J. Wang, H. Y. Deng, X. Li, C. Yang and Y. Xia, *Sens. Actuators, B*, 2019, **304**, 127317.
- 73 Y. Kang, S. Pyo, E. Jo and J. Kim, *Nanotechnology*, 2019, **30**, 355504.
- 74 M. Donarelli, S. Prezioso, F. Perrozzi, F. Bisti, M. Nardone, L. Giancaterini, C. Cantalini and L. Ottaviano, *Sens. Actuators, B*, 2015, **207**, 602–613.
- 75 J. H. Zhang, T. T. Li, J. Y. Guo, Y. Q. Hu and D. Z. Zhang, *Appl. Surf. Sci.*, 2021, **568**, 150942.
- 76 X. Chang, X. F. Li, X. R. Qiao, K. Li, Y. X. Li, T. C. Guo, L. Zhu and Q. Z. Xue, *Sens. Actuators, B*, 2019, **304**, 127430.
- 77 Y. T. Han, Y. J. Ma, Y. Liu, S. S. Xu, X. W. Chen, M. Zeng, N. T. Hu, Y. J. Su, Z. H. Zhou and Z. Yang, *Appl. Surf. Sci.*, 2020, **493**, 613–619.
- 78 D. H. Baek, G. Choi, Y. Kwak, B. H. Cho and J. Kim, Proceedings of the IEEE International Conference on Micro Electro Mechanical Systems (MEMS), 2019 IEEE 32nd International Conference on Micro Electro Mechanical Systems, MEMS 2019, 2019, pp. 468–471.
- 79 Y. N. Liu, S. Li, S. Xiao and K. Du, *Colloids Surf., A*, 2022, **648**, 129435.
- 80 P. X. Zhao, Y. Tang, J. Mao, Y. X. Chen, H. Song, J. W. Wang, Y. Song, Y. Q. Liang and X. M. Zhang, *J. Alloys Compd.*, 2016, **674**, 252–258.
- 81 R. Kumar, N. Goel, M. Mishra, G. Gupta, M. Fanetti, M. Valant and M. Kumar, *Adv. Mater. Interfaces*, 2018, **5**, 1800071.
- 82 S. Sharma, A. Kumar, N. Singh and D. Kaur, *Sens. Actuators, B*, 2018, **275**, 499–507.
- 83 Y. Xiong, W. D. Liu, K. C. Wu, T. Liu, Y. M. Chen, X. Z. Wang and J. Tian, *J. Alloys Compd.*, 2022, **927**, 166962.
- 84 D. Z. Zhang, Y. B. Jin and Y. H. Cao, *J. Mater. Sci.: Mater. Electron.*, 2019, **30**, 573–581.
- 85 Y. Q. Ding, X. Z. Guo, B. S. Du, X. F. Hu, X. Yang, Y. He, Y. Zhou and Z. G. Zang, *J. Mater. Chem. C*, 2021, **9**, 4838–4846.
- 86 H. Yan, M. J. Zhong, Z. Lv and P. B. Wan, *Small*, 2017, **13**, 1701697.
- 87 S. Ahmad, I. Khan, A. Husain, A. Khan and A. M. Asiri, *Polymer*, 2021, **12**, 3047.
- 88 X. Bai, H. Lv, Z. Liu, J. K. Chen, J. Wang, B. H. Sun, Y. Zhang, R. H. Wang and K. Y. Shi, *J. Hazard. Mater.*, 2021, **416**, 125830.
- 89 D. Z. Zhang, C. X. Jiang, P. Li and Y. E. Sun, *ACS Appl. Mater. Interfaces*, 2017, **9**, 6462–6471.
- 90 J. Sun, N. Lin, H. Ren, C. Tang, L. T. Yang and X. Zhao, *RSC Adv.*, 2016, **6**, 17494–17503.
- 91 M. Ikram, L. J. Liu, Y. Liu, L. F. Ma, H. Lv, M. Ullah, L. He, H. Y. Wu, R. H. Wang and K. Y. Shi, *J. Mater. Chem. A*, 2019, **7**, 14602–14612.
- 92 S. Dhara, H. Jawa, S. Ghosh, A. Varghese, D. Karmakar and S. Lodha, *ACS Appl. Mater. Interfaces*, 2021, **13**, 30785–30796.
- 93 S. H. Zhang, J. Y. Wang, N. L. Torad, W. Xia, M. A. Aslam, Y. V. Kaneti, Z. F. Hou, Z. J. Ding, B. Da and A. Fatehmulla, *Small*, 2019, **16**, 1901718.
- 94 G. Liu, S. L. Rumyantsev, C. Jiang, M. S. Shur and A. A. Balandin, *IEEE Electron Device Lett.*, 2015, **36**, 1202–1204.
- 95 V. Le, Y. Vasseghian, V. Doan, T. T. T. Nguyen, T. T. T. Vo, K. B. Vu, Q. H. Vu, T. D. Lam and V. A. Tran, *Chemosphere*, 2022, **291**, 133025.
- 96 R. Zen, Y. B. Shi, T. M. Song, T. Wang, B. L. Tang, H. D. Niu and X. Y. Yu, *Chemosphere*, 2022, **9**, 345.
- 97 W. B. Li, H. Li, R. Qian, S. J. Zhuo, P. F. Ju and Q. Chen, *Nanomaterials*, 2022, **12**, 1300.
- 98 C. Yang, Y. Y. Wang, Z. K. Wu, Z. B. Zhang, N. T. Hu and C. S. Peng, *Nanomaterials*, 2022, **12**, 901.
- 99 I. Jahangir, M. A. Uddin, A. K. Singh, M. V. S. Chandrashekhar and G. Koley, *IEEE Sens. J.*, 2021, **21**, 26549–26555.
- 100 W. Zheng, Y. S. Xu, L. L. Zheng, C. Yang, N. Pinna, X. H. Liu and J. Zhang, *Adv. Funct. Mater.*, 2020, **30**, 2000435.
- 101 H. Yan, L. H. Chu, Z. Li, C. X. Sun, Y. X. Shi and J. Ma, *Sensors and Actuators Reports*, 2022, **4**, 100103.
- 102 F. Schedin, A. K. Geim, S. V. Morozov, E. W. Hill, P. Blake, M. I. Katsnelson and K. S. Novoselov, *Nat. Mater.*, 2007, **6**, 652–655.



- 103 M. Sangeetha and D. Madhan, *Opt. Laser Technol.*, 2020, **127**, 106193.
- 104 J. D. Fowler, M. J. Allen, V. C. Tung, Y. Yang, R. B. Kaner and B. H. Weiller, *ACS Nano*, 2009, **3**, 301–306.
- 105 F. L. Meng, Z. Guo and X. J. Huang, *TrAC, Trends Anal. Chem.*, 2015, **68**, 37–47.
- 106 S. Singh and S. Sharma, *Mater. Today*, 2021, **45**, 4910–4913.
- 107 T. Xie, G. Z. Xie, Y. J. Su, H. F. Du, Z. B. Ye and Y. D. Jiang, *Nanotechnology*, 2016, **27**, 065502.
- 108 M. Ikram, H. Lv, Z. Liu, M. Khan, L. J. Liu, F. Raziq, X. Bai, M. Ullah, Y. Zhang and K. Y. Shi, *Chem. Mater.*, 2020, **32**, 7215–7225.
- 109 X. Xin, Y. Zhang, X. Guan, J. Cao, W. Li, X. Long and X. Tan, *ACS Appl. Mater. Interfaces*, 2019, **11**, 9438–9447.
- 110 N. Goel, R. Kumar, S. K. Jain, S. Rajamani, B. Roul, G. Gupta, M. Kumar and S. B. Krupanidhi, *Nanotechnology*, 2019, **30**, 314001.
- 111 J. Jaiswal, A. Sanger, P. Tiwari and R. Chandra, *Sens. Actuators, B*, 2020, **305**, 127437.
- 112 C. Liu, X. W. Chen, H. Y. Luo, B. L. Li, J. Shi, C. Fan, J. H. Yang, M. Zeng, Z. H. Zhou and N. T. Hu, *Sens. Actuators, B*, 2021, **347**, 130608.
- 113 J. B. Liu, J. Y. Hu, C. Liu, Y. M. Tan, X. Peng and Y. Zhang, *Rare Met.*, 2020, **40**, 1536–1544.
- 114 X. Tian, L. J. X. X. Cui, R. J. Zhao, T. Chen, X. C. Xiao and Y. D. Wang, *J. Mater. Chem. A*, 2022, **10**, 5505–5519.
- 115 Y. Q. Ding, X. Z. Guo, D. L. Kuang, X. F. Hu, Y. Zhou, Y. He and Z. G. Zang, *J. Hazard. Mater.*, 2021, **416**, 126218.
- 116 Q. Yue, Z. Z. Shao, S. L. Chang and J. B. Li, *Nanoscale Res. Lett.*, 2013, **8**, 425.
- 117 W. F. Jiang, K. F. Chen, J. W. Wang, D. Geng, N. A. D. Lu and L. Li, *Mater. Res. Express*, 2021, **8**, 055010.
- 118 Y. T. Han, D. Huang, Y. G. Ma, G. L. He, J. Hu, J. Zhang, N. T. Hu, Y. J. Su, Z. H. Zhou, Y. F. Zhang and Z. Yang, *ACS Appl. Mater. Interfaces*, 2018, **10**, 22640–22649.
- 119 A. P. Lee and B. J. Reedy, *Sens. Actuators, B*, 1999, **60**, 35–42.
- 120 N. Barsan and U. Weimar, *J. Electroceram.*, 2001, **7**, 143–167.
- 121 D. Z. Zhang, Y. E. Sun, C. X. Jiang, Y. Yao, D. Y. Wang and Y. Zhang, *Sens. Actuators, B*, 2017, **253**, 1120–1128.
- 122 D. Z. Zhang, J. F. Wu, P. Li and Y. H. Cao, *J. Mater. Chem. A*, 2017, **5**, 20666–20677.
- 123 Y. Fu, J. Z. Li and H. Y. Xu, *Mater. Sci. Semicond. Process.*, 2020, **114**, 105073.
- 124 Y. S. Shim, K. C. Kwon, J. M. Suh, K. S. Choi, Y. G. Song, W. Sohn, S. Choi, K. Hong, J. M. Jeon and S. P. Hong, *ACS Appl. Mater. Interfaces*, 2018, **10**, 31594–31602.
- 125 B. L. Liu, L. Chen, G. Liu, A. N. Abbas, M. Fathi and C. W. Zhou, *ACS Nano*, 2014, **8**, 5304–5314.
- 126 T. T. Xu, Y. Y. Pei, Y. Y. Liu, D. Wu, Z. F. Shi, J. M. Xu, Y. T. Tian and X. J. Li, *J. Alloys Compd.*, 2017, **725**, 253–259.
- 127 H. H. Hau, T. T. H. Duong, N. K. Man, T. T. V. Nga, C. T. Xuan, D. T. T. Le, N. V. Toan, C. M. Hung, N. V. Duy, N. V. Hieu and N. D. Hoa, *Sens. Actuators, A*, 2021, **332**, 113137.
- 128 S. Y. Cho, S. J. Kim, Y. Lee, J.-S. Kim, W. B. Jung, H. W. Yoo, J. Kim and H. Jung, *ACS Nano*, 2015, **9**, 9314.
- 129 R. Kumar, P. K. Kulriya and M. Kumar, *Nanotechnology*, 2018, **29**, 464001.
- 130 R. Kumar, N. Goel and M. Kumar, *ACS Sens.*, 2017, **2**, 1744–1752.
- 131 P. Chen, J. Y. Hu and Y. Zhang, *ACS Appl. Mater. Interfaces*, 2021, **4**, 5981–5991.
- 132 K. Rathi, A. N. Kumar and K. Pal, *Nanotechnology*, 2020, **31**, 395504.
- 133 P. Bharathi, S. Harish, G. Mathankumar, M. K. Mohan, J. Archana, S. Kamalakannan, M. Prakash, M. Shimomura and M. Navaneethan, *Appl. Surf. Sci.*, 2022, **600**, 154086.
- 134 H. E. Bai, H. Guo, C. Feng, J. Wang, B. Liu, Z. L. Xie, F. Q. Guo, D. J. Chen, R. Zhang and Y. D. Zheng, *Sens. Actuators, B*, 2022, **368**, 132131.
- 135 Z. M. Yang, D. Z. Zhang and H. N. Chen, *Sens. Actuators, B*, 2019, **300**, 127037.
- 136 M. Ikram, L. Liu, Y. Liu, M. Ullah, L. Ma and S. U. H. Bakhtiar, *Nanoscale*, 2019, **11**, 8554–8564.
- 137 L. J. Liu, M. Ikram, L. F. Ma, X. Y. Zhang, H. Lv, M. Ullah, M. Khan, H. T. Yu and K. Y. Shi, *J. Hazard. Mater.*, 2020, **393**, 122325.
- 138 Q. N. Zhao, W. Z. Zhou, M. X. Zhang, Y. Wang, Z. H. Duan, C. L. Tan, B. H. Liu, F. P. Ouyang, Z. Yuan and H. L. Tai, *Adv. Funct. Mater.*, 2022, **32**, 2203528.
- 139 N. Kanaujiya, A. K. Golimar, P. C. Pandey and J. G. D. Varma, *AIP Conf. Proc.*, 2018, **1953**, 030142, DOI: [10.1063/1.5032477](https://doi.org/10.1063/1.5032477).
- 140 A. Taufik, Y. Asakura, T. Hasegawa and S. Yin, *ACS Appl. Nano Mater.*, 2021, **4**, 6861–6871.
- 141 S. Ramu, T. Chandrakalavathi, G. Murali, K. S. Kumar, A. Sudharani, M. Ramanadha, K. R. Peta, R. Jeyalakshmi and R. P. Vijayalakshmi, *Mater. Res. Express*, 2019, **6**, 085075.
- 142 S. Y. Hou, R. Pang, S. L. Chang, L. Ye, J. Xu, X. C. Wang, Y. J. Zhang, Y. Y. Shang and A. Y. Cao, *ACS Appl. Mater. Interfaces*, 2020, **12**, 29778–29786.
- 143 D. Wu, Z. H. Lou, Y. G. Wang, T. T. Xu, Z. F. Shi, J. M. Xu, Y. T. Tian and X. J. Li, *Nanotechnology*, 2017, **28**, 435503.
- 144 X. X. He, Z. H. Ying, F. Wen, L. L. Li, X. L. Zheng, P. Zheng and G. F. Wang, *Mater. Sci. Semicond. Process.*, 2021, **134**, 105997.
- 145 Y. P. Miao, H. W. Bao, W. Fan, Y. Li and F. Ma, *Surf. Interfaces*, 2021, **27**, 101580.
- 146 B. Zhao, C. Y. Li, L. L. Liu, B. Zhou, Q. K. Zhang, Z. Q. Chen and Z. Tang, *Appl. Surf. Sci.*, 2016, **382**, 280–287.
- 147 S. Sharma, A. Kumar and D. Kaur, *AIP Conf. Proc.*, 2018, **1953**, 030261.
- 148 S. Singh and S. Sharma, *AIP Conf. Proc.*, 2021, **2265**, 030690.
- 149 D. Z. Zhang, C. X. Jiang and Y. E. Sun, *J. Alloys Compd.*, 2017, **698**, 476–483.
- 150 S. Singh, S. Sharma, R. C. Singh and S. Sharma, *Appl. Surf. Sci.*, 2020, **532**, 147373.
- 151 S. Singh, R. M. Sattigeri, S. Kumar, P. K. Jha and S. Sharma, *ACS Omega*, 2021, **6**, 11602–11613.
- 152 A. Liu, S. Y. Lv, L. Jiang, F. M. Liu, L. J. Zhao, J. Wang, X. L. Hu, Z. J. Yang, J. M. He, C. G. Wang and G. Y. Lu, *Sens. Actuators, B*, 2021, **332**, 129444.



- 153 A. Q. Jian, J. H. Wang, H. Y. Lin, S. Q. Xu, D. Han, Z. Y. Yuan and K. Zhuo, *ACS Omega*, 2022, **7**, 11664–11670.
- 154 S. Singh, J. Deb, U. Sarkar and S. Sharma, *ACS Sustainable Chem. Eng.*, 2021, **9**, 7328–7340.
- 155 D. Z. Zhang, Z. L. Wu, P. Li, X. Q. Zong, G. K. Dong and Y. Zhang, *Sens. Actuators, B*, 2018, **258**, 895–905.
- 156 K. J. Yoon, S. I. Lee, H. An, J. Kim, J. W. Son, J. H. Lee, H. J. Je, H. W. Lee and B. K. Kim, *Int. J. Hydrogen Energy*, 2014, **39**, 3868–3878.
- 157 S. E. Hosseini and M. A. Wahid, *Renewable Sustainable Energy Rev.*, 2016, **57**, 850–866.
- 158 M. M. Y. A. Alsaif, S. Balendhran, M. R. Field, K. Latham, W. Wlodarski, J. Z. Ou and K. K. Zadeh, *Sens. Actuators, B*, 2014, **192**, 196–204.
- 159 F. K. Perkins, A. L. Friedman, E. Cobas, P. M. Campbell, G. G. Jernigan and B. T. Jonker, *Nano Lett.*, 2013, **13**, 668–673.
- 160 M. V. Bollinger, J. V. Lauritsen, K. W. Jacobsen, J. K. Nørskov, S. Helveg and F. Besenbacher, *Phys. Rev. Lett.*, 2001, **87**, 196803.
- 161 K. Dolui, I. Rungger and S. Sanvito, *Phys. Rev. B: Condens. Matter Mater. Phys.*, 2013, **87**, 165402.
- 162 A. Castellanos-Gomez, N. Agrait and G. Rubio-Bollinger, *Appl. Phys. Lett.*, 2010, **96**, 213116.
- 163 Z. Zhang, K. Chen, Q. Zhao, M. Huang and X. P. Ouyang, *Mater. Res. Express*, 2020, **7**, 015501.
- 164 D. H. Baek and J. Kim, *Sens. Actuators, B*, 2017, **250**, 686–691.
- 165 H. D. Mai, S. Jeong, T. K. Nguyen, J. S. Youn, S. Ahn, C. M. Park and K. J. Jeon, *ACS Appl. Mater. Interfaces*, 2012, **13**, 14657–14665.
- 166 S. L. Yang, G. Lei, Z. G. Lan, W. Xie, B. P. Yang, H. X. Xu, Z. Wang and H. S. Gu, *Int. J. Hydrogen Energy*, 2019, **44**, 7725–7733.
- 167 W. Wu, Z. Liu, L. A. Jauregui, Q. Yu, R. Pillai, H. Cao, J. Bao, Y. P. Chen and S. S. Pei, *Sens. Actuators, B*, 2010, **150**, 296–300.
- 168 C. Pijolat, G. Tournier, P. Breuil, D. Matarin and P. Nivet, *Sens. Actuators, B*, 2002, **82**, 166–175.
- 169 C. M. Wu, K. G. Motora, G. Y. Chen, D. H. Kuo and N. S. Gultom, *Front. Mater. Sci.*, 2022, **9**, 831725.
- 170 A. Saravanan, B. R. Huang, J. P. Chu, A. Prasannan and H. C. Tsai, *Sens. Actuators, B*, 2019, **292**, 70–79.
- 171 D. Kathiravan, B. R. Huang, A. Saravanan, A. Prasannan and P. D. Hong, *Sens. Actuators, B*, 2019, **279**, 138–147.
- 172 (a) A. Venkatesan, S. Rathi, I. Y. Lee, J. Park, D. Lim, M. Kang, H. I. Joh, G. H. Kim and E. S. Kannan, *Nanotechnology*, 2017, **28**, 365501.
- 173 D. Z. Zhang, Y. E. Sun, C. X. Jiang and Y. Zhang, *Sens. Actuators, B*, 2017, **242**, 15–24.
- 174 L. Z. Hao, Y. J. Liu, W. Gao, Y. M. Liu, Z. D. Han, L. Q. Yu, Q. Z. Xue and J. Zhu, *J. Alloys Compd.*, 2016, **682**, 29–34.
- 175 A. V. Agrawal, R. Kumar, S. Venkatesan, A. Zakhidov, Z. Zhu, J. M. Bao and M. Kumar, *Appl. Phys. Lett.*, 2017, **111**, 093102.
- 176 S. L. Yang, Z. Chen, Z. Wang, G. Lei, J. Xiong, H. X. Xu and H. S. Gu, *Sens. Actuators, B*, 2022, **367**, 132026.
- 177 V. Munusami, K. Arutselvan, S. Vadivel and S. Govindasamy, *Ceram. Int.*, 2022, **48**, 29322–29331.
- 178 A. K. Vivekanandan, B. R. Huang, D. Kathiravan, A. Saravanan, A. Prasannan, H. C. Tsai and S. H. Chen, *J. Alloys Compd.*, 2021, **854**, 157102.
- 179 J. F. Wu, D. Z. Zhang and Y. H. Cao, *J. Colloid Interface Sci.*, 2018, **529**, 556–567.
- 180 B. Chakraborty, I. Maity, P. Chung, M. Ho and P. Bhattacharyya, *IEEE Sens. J.*, 2021, **21**, 16484–16491.
- 181 X. X. Deng, X. Y. Liang, S. P. Ng and C. M. L. Wu, *Appl. Surf. Sci.*, 2019, **484**, 1244–1252.
- 182 D. Z. Zhang, C. X. Jiang and X. Y. Zhou, *Talanta*, 2018, **182**, 324–332.
- 183 D. Z. Zhang, X. Fan, A. J. Yang and X. Q. Zong, *J. Colloid Interface Sci.*, 2018, **523**, 217–225.
- 184 X. Li, J. Wang, D. Xie, J. L. Xu, Y. Xia, L. Xiang and S. Komarneni, *Mater. Lett.*, 2017, **189**, 42–45.
- 185 D. Z. Zhang, C. X. Jiang and J. F. Wu, *Sens. Actuators, B*, 2018, **273**, 176–184.
- 186 X. Li, J. Wang, D. Xie, J. L. Xu, Y. Xia, W. W. Li, L. Xiang, Z. M. Li, S. W. Xu and S. Komarneni, *Nanotechnology*, 2017, **28**, 325501.

